Charles University in Prague
Faculty of Mathematics and Physics

Doctoral Thesis

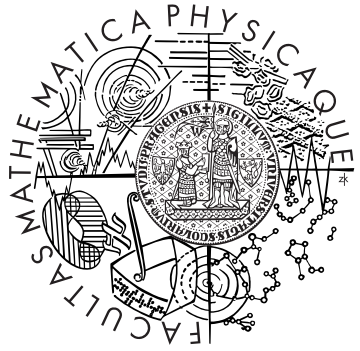

RNDr. Ladislav Fekete

Ultrafast carrier dynamics in semiconductors studied by Time-resolved terahertz spectroscopy

Supervisor: RNDr. Petr Kužel, Dr

Prague, 2008

Acknowledgments

I would like to thank to everybody without whom this thesis would not have been written. Especially my supervisor, Petr Kužel, for introducing me into the topic, for his patient guidance, support and the critical reading of the present manuscript which resulted in great improvement of the thesis; Hynek Němec and Filip Kadlec for fruitful discussions, guidance and helping me in the laboratory and all the members of the Terahertz group for the helpful and friendly atmosphere.

I would like also to thank employees of the Czech Academy of Sciences, namely Antonín Fejfar for discussions about the interpretation of data of the μc-Si, Jiří Stuchlík for the preparation of the μc-Si samples, Martin Ledinský for help with Raman measurements, Dagmar Chvostová for the profilometry measurements, Alexander Dejneka for ellipsometry measurements and Jiří Fryštacký for the polishing of the PC platelets.

Moreover, I am grateful to Patrik Mounaix and Jean-Christophe Delagnes from Université Bordeaux for the assistance with the interpretation of the InP measurements and I am indebted to Juliette Mangeney from Institut d'Electronique Fondamentale in France for providing me with InP samples.

My special thanks belong to Kateřina Kůsova for patience during corrections and for being there for me every time I needed help.

I hereby state that I have written the thesis by myself using only the cited references. I agree with lending of the thesis.

Prague, 20^{th} December 2008 Ladislav Fekete

Abstract

The thesis is devoted to the study of the interaction of THz radiation with photoexcited carriers in semiconductors and it focuses on the investigation of the photocarrier dynamics on the subpicosecond to nanosecond timescales. The experimental technique – time-resolved THz spectroscopy – involves the generation and sensitive detection of ultrafast broadband THz pulses and allows one to determine the time resolved far-infrared (THz) complex conductivity spectra of photoexcited samples. The interpretation is provided in terms of carrier lifetimes, transport properties (band-like versus hopping) and degree of localization.

We studied the ultrafast response of two different semiconductors, namely radiation-damaged indium phosphide and microcrystalline silicon. In the first case we have shown that irradiation of InP wafers by high-energy heavy-ions (Br^+) dramatically reduces the lifetime of carriers: down to 300 fs for the most irradiated sample, i.e. 3 orders of magnitude compared to as-grown sample. At the same time the carrier mobility dropped by the factor of 3.

In the second case we investigated nanoscopic transport properties of thin film silicon samples with a crystallinity varying from amorphous to fully microcrystalline. The initial transient photoconductivity of the samples was dominated by hot free carriers which were trapped into weakly localized hopping states after 0.6 ps, on the sub-nanosecond scale the charge transport was found to be dominated by hopping.

The last part of our studies was focused on the possibility to achieve an optical control of the THz beam propagation. For that purpose we have designed and studied the response of fast modulators, where the opto-THz coupling was induced by optical injection of carriers in semiconductor layer. The interaction of the THz pulse with free carriers was enhanced by putting the layer into a photonic-crystal.

Preface

Terahertz (THz) radiation, with frequencies from approximately 100 GHz to 10 THz, fills the gap between the infrared domain and microwaves. This region was for a long time impossible to reach, as the THz frequencies were too high to be generated by electronic synthesizers and too low for optical sources. The breakthrough in the generation of THz frequencies was tightly connected to the development of femtosecond lasers. Subsequently, the development of the time-domain THz spectroscopy (and the time-resolved THz spectroscopy as its specific application for ultrafast phenomena studies) allowed for the investigation of materials and structures exhibiting a fingerprint response in the THz range.

Semiconductors, which constitute the main subject of this thesis, are one of the most studied types of materials in this spectral region. Due to their ultrafast carrier lifetime and high mobilities they have been kept under surveillance of scientists since the early beginnings of the THz research as materials suitable for THz emitters and detectors.

Time-resolved THz spectroscopy is a contact-free probing method which allows one to access the complex THz spectral response of semiconductors and its ultrafast subpicosecond to nanosecond time evolution induced upon photoexcitation. The shape of the spectral response, expressed typically as complex conductivity or permittivity, characterizes the nature of the carrier transport on the nanoscopic scale ($\lesssim 100$ nm). This makes the method highly suitable for the investigation of the charge transport in disordered systems, such as amorphous, microcrystalline or radiation-damaged semiconductors.

Today, THz technology is finding its use in many applications ranging from biology and medical science, quality control of food, homeland security to information and communication technology and ultrafast computing. The need of processing the THz radiation involves the development of new tools such as agile switches, modulators, and phase shifters. THz modulators can be described as structures which contain a medium with a strong THz response controllable by an external parameter (like electric field or optical pulse). They may also contain a resonant element (e.g. a photonic crystal). Without a resonant element, a broadband response of the device can be often achieved. However, a strong interaction may be frequently required to obtain appreciable modulation effects even for small values of the control parameter. The resonant element can dramatically enhance the interaction strength at the price of a significant narrowing of the useful bandwidth of the device. High-resistivity semiconductors show big potential for the optical control of their reflectance or transmittance in the THz spectral range. With their transparency in steady state and high absorption of THz radiation in the photoexcited state they represent an ideal candidate for the key-elements in which the propagation of THz waves is controlled by the intensity of the photoexcitation.

This work has the following structure. In the first Chapter after a short introduction a review of the principles of THz generation and detection and the most prominent THz applications will be exposed. In Chapter 2 our experimental setup and the fundamentals of

the ultrafast THz spectroscopy will be presented along with the mathematical apparatus for the description of the propagation of THz pulses in photoexcited media. The original part of the work is summarized in Chapter 3. This chapter is a resume of the of author's publications in impacted journals, presented in the Appendix, which are denoted as [i-vi]. Here, the research on two different semiconductors, namely radiation-damaged InP and microcrystalline silicon, is introduced. The third part of Chapter 3 represents the development of an opto-THz switch and modulator.

Contents

Abstract **1**

Preface **2**

Contents **4**

1 Terahertz radiation **7**
1.1 Introduction 7
1.2 THz sources 9
1.2.1 Biased and unbiased photoconductive switches 10
1.2.2 Optical rectification 12
1.2.3 Cerenkov-like emission of THz radiation 13
1.2.4 Tunable THz-wave parametric generation 15
1.2.5 Quantum cascade lasers 17
1.2.6 Backward wave oscillators 19
1.2.7 Free electron lasers and synchrotrons 20
1.2.8 Coherent THz Radiation from Superconductors 21
1.2.9 Terahertz radiation from shocked materials 21
1.3 THz detectors 21
1.3.1 Photoconductive receiving antennas 22
1.3.2 Electrooptic sampling 23
1.3.3 Magnetooptic sampling 25
1.3.4 Terahertz-induced lensing 25
1.3.5 Bolometers 26
1.4 THz applications 27
1.4.1 Astronomy 28
1.4.2 Electrical integrated circuits inspection 29
1.4.3 Narcotics inspection 29
1.4.4 Explosives and weapons detection 30

2 Time-domain THz spectroscopy **31**
2.1 Introduction . . . 31
2.2 Experimental setup . . . 31
2.3 Methods of the time-domain THz spectroscopy . . . 36
2.3.1 Steady-state spectroscopy . . . 36
2.3.1.a Transmission spectroscopy . . . 36
2.3.1.b Reflection spectroscopy . . . 40
2.3.2 Time-resolved spectroscopy . . . 40
2.3.2.a Emission spectroscopy . . . 41
2.3.2.b Optical-pump THz-probe spectroscopy . . . 41
2.3.3 Models of slow dynamics conductivity . . . 45
2.3.4 Drude model . . . 46
2.3.5 Relaxator model . . . 46
2.3.6 Hopping model . . . 46
2.4 Models of fast dynamics conductivity . . . 47
2.4.1 Drude model . . . 47
2.4.2 Overdamped relaxator model . . . 47

3 THz spectroscopy of semiconductors **49**
3.1 Ultrafast carrier dynamics in InP . . . 51
3.2 Microcrystalline silicon . . . 54
3.3 Active optical control of the THz reflectivity of high-resistivity semiconductors 57
3.3.1 GaAs wafer modulator . . . 58
3.3.2 Photonic-crystal opto-THz modulator . . . 60
3.4 Outlook . . . 66
3.5 Summary . . . 67

References **69**

Appendix **78**

Chapter 1

Terahertz radiation

1.1 Introduction

Terahertz (THz) radiation is a part of the electromagnetic spectrum which covers frequencies between 10^{11} Hz and 10^{13} Hz. This region borders with microwaves at the low-energy end and infrared at the high-energy end (see Fig. 1.1). The radiation in this spectral region is invisible to the naked eye. It is low-energy non-destructive non-ionizing radiation (1 THz = 4 meV), and therefore it does not pose a threat to human body. On the contrary, as 1 THz corresponds to the black-body radiation at 48 K, all living objects, which are in fact much hotter, are sources of THz radiation. The interaction of THz waves with matter has several specific features. On the one hand, it penetrates non-conductive materials such as paper, plastics, wood, clothing and ceramics. On the other hand, it can be easily stopped by metals or water. For commercial and security applications it is not irrelevant that narcotics, explosives and other chemical substances have unique spectral features (fingerprints) in this range of frequencies.

Surprisingly, the exploration boom of the THz region started only some 20 years ago thanks to D. Grischowsky (at IBM) and D. Auston (at Bell Labs) [1] [2]. They introduced a new method for the production and detection of bright coherent THz pulses using ultrafast electric pulses. Their experiments with the generation and detection of THz radiation were in fact remarkably similar to famous Hertz's experiments 100 years ago, which Hertz used for the validation of Maxvell's equations: the acceleration of charge that resulted from a spark jumping the gap between two brass electrodes emitted a freely propagating electromagnetic wave that caused a spark to jump a similar gap in a detector placed on the other side of the room. Hertz performed this dipole radiation experiments to study polarization, refraction and reflection in order to show that electricity can propagate as a wave. Even though the way of producing dipole radiation used in 1980s, where a biased high-resistivity semiconductor was illuminated via ultrashort laser pulses, was much more sophisticated, the underlying physical principles were the same.

Nowadays, this method of the generation and detection of THz radiation is widespread and used in many laboratories. However, it is not the only possibility. Broad-band THz radiation can be produced using ultrafast lasers also via other methods like optical rectification in non-linear crystals such as ZnTe or at metal surfaces. Furthermore, backward-wave oscillators or optically pumped FIR gas lasers (methanol laser) are classical sources of monochromatic THz radiation, while new possibilities can lie for example in the use of Josephson effect in biased stack of high-temperature superconducting crystals (so-called Josephson junctions), in quantum-cascade lasers or in shocked materials. Moreover, high-intensity THz radiation is produced in synchrotrons, linear accelerators or free electron lasers.

As researchers have been conquering the THz battlefield only for a short time, so far only a small fraction of possible applications is commercially available nowadays. Nevertheless, their progress is rapid and an enormous variety of possibilities lie in front of them. The terahertz science is not only abstract fundamental research of different types of solid-state materials, gasses, liquids, chemicals or sophisticated materials like superconductors, ferroelectrics and semiconductors, but it is also slowly fighting its way to the "real" world. For example the amount of data people exchange is shifting the speed of telecommunication from units of GHz to tens and hundreds of GHz, which is attacking the lower edge of THz region. This border has recently been experimentally crossed. However, further progress is slowed down not only by the lack of low-cost ultrafast electronic emitters and receivers but also by the lack of ultrafast devices for encoding information, such as switches or modulators. In addition, terahertz research has joined the still-loosing fight

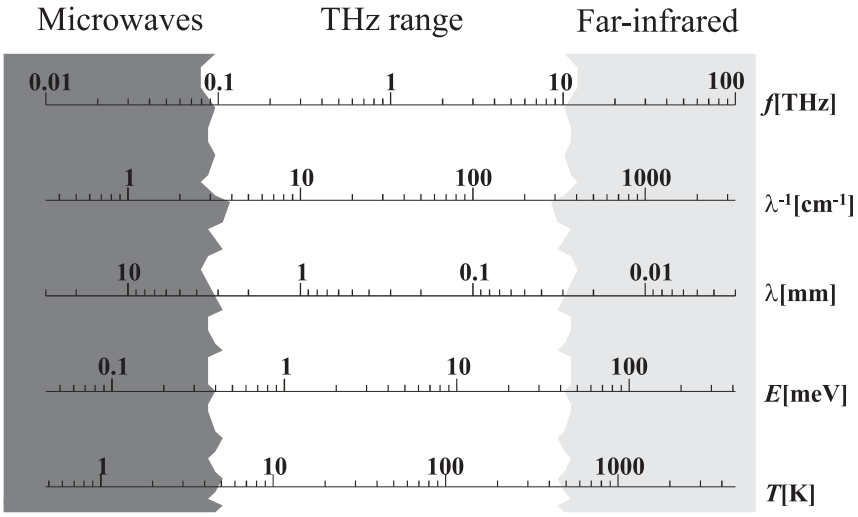

Figure 1.1: Spectrum of electromagnetic radiation. The THz gap is marked by a green rectangle.

with cancer and the fight with dental caries. The flagship of terahertz research is, however, fighting under the colors of security. Airport scanners uncovering hidden objects (metal or ceramic weapons) are being tested, devices which can sense explosives from a 40-meter distance were demonstrated. Thus, terahertz research is pushing further frontiers of the fundamental research and it has the potential to make our lives more simple and secure in the future.

1.2 THz sources

For a long time, the THz part of the electromagnetic spectrum was only very difficult to access. The main reason for this situation was that only a few sources of THz radiation were available and they were producing weak signals. The revolution in this field began with the development of femtosecond lasers, which allowed researches to find new ways of generating the THz frequencies to make the THz region more accessible. Moreover, various materials could be characterized and subsequently used as THz sources or as the laser media. Another mechanism of the THz generation uses oscillations of an accelerated electron beam.

In this section, several types of the generation of THz radiation will be introduced. For a better overview they can be organized into subsections according to the type of radiation they produce or according to the principle of generation:

Characteristics	*Method*
Pulsed broadband	Photoconductive switches
	Optical rectification
	Cerenkov-like radiation
Pulsed tunable	THz-wave parametric generators
Monochromatic	Backward wave oscillators
	Quantum cascade lasers
Large scale facilities	Free electron lasers
	Synchrotrons
Novel sources	Shocked materials
	Superconductors

Besides this methods of the generation there can be found in the literature other methods such as black body radiation sources - used in Fourier transform infrared spectroscopy apparatuses, p-Ge lasers, photomixing, multiplication of GHz frequencies or optically pumped far-infrared lasers. These sources produce incoherent or weak THz radiation, they are too complicated or they are only rarely used in the THz region of electromagnetic radiation.

1.2.1 Biased and unbiased photoconductive switches

The basic idea of a semiconductor emitter with a biased electrode structure is relatively young [2]. The semiconductor material is illuminated in the area between the electrodes by ultrashort (100 fs) pulses with photon energy exceeding the bandgap energy. Free carriers created in this process are accelerated by applied voltage, where the rapid variation of the current density gives rise to a pulse of THz radiation emitted into the substrate (Fig. 1.2a). Finally, the carriers are trapped or recombine and the current density returns to its steady-state value. The lifetime of free carriers plays a significant role, because the emitter has to reach a steady-state before the next excitation pulse. In pure monocrystalline materials the lifetime of photogenerated free carriers is longer or comparable to the timescale of interest. On the other hand, semiconductor materials with mobile carriers where their lifetimes are reduced to sub-picosecond scales – radiation-damaged silicon-on-sapphire (RD-SOS) [2, 3] or low-temperature-grown GaAs (LT-GaAs) [4] – have better performances, because the current flows for a reduced amount of time which is comparable with the duration of THz pulses.

The light absorption process in photoconductive switches saturates at low pump intensities. At high pump intensities, the pump pulse penetrates deep inside the semiconductor and free carriers generated far from the surface absorb the THz radiation produced near the surface. Thus, the overall efficiency of the generation of THz radiation does not increase proportionally to the pump intensity. Therefore photoconductive emitters are more suitable for non-amplified femtosecond laser systems.

Several types of semiconductor-emitter configurations can be found. The historically first scheme was a small-aperture antenna (Fig. 1.2c). In this case the electrodes are separated typically by several tens of microns and the wavelength of THz radiation is larger than the aperture of the emitter. These devices can be well approximated by an elementary Hertzian dipole, where the on-axis radiated field far from the dipole is given by the time derivative of the current density. This technology allows for the use of relatively low-power laser sources (energy per pulse <1 nJ) and low voltages can be applied to the electrodes of the antenna (typically tens of volts). A common property of these kinds of sources is high divergence. Thus, a collimating lens attached directly to the emitter is used to enhance the radiated power in the forward direction [5].

Later, a large-aperture emitter scheme, which did not need a collimation lens, was extensively used (Fig. 1.2b). The main advantage of this scheme was that higher voltages (units of kV) could be used, which led to higher emitted THz power. These antenna structures can be approximated by a superposition of elementary dipoles [6] reducing the dipole divergence. Moreover, the increase of the size of the emitter area made the absorption of the entire optical radiation possible without the problems of damage and saturation, thus this type of emitter could also be used with higher-power lasers. The output THz electric field scales linearly with optical fluences and for 1 mJ/cm^2 the THz peak field as large as 1.2 kV/cm was observed [7].

The next step in the evolution of this type of emitter was introduced in [8]. The photoconducting antenna emitter consists of an integrated metal electrode metal-semiconductor-metal (MSM) structure. The electrodes prepared on a surface of a semiconductor have a finger-like structure, where every second period is blocked by another metallization layer isolated from the MSM electrodes (see Fig 1.3). This metallization blocks the optical excitation radiation and consequently allows the generation of carriers only in the parts of the emitter with the same orientation of the bias electric field. The whole device can be decomposed to a large number of small emitters simultaneously emitting THz radiation in phase. Thus the emitted THz radiation interferes constructively in far field. Relatively high THz electric field output with amplitudes in orders of hundreds of V/cm can be achieved by using femtosecond oscillator with average power of 600 mW and 5 nJ/pulse and only small bias voltage (20 V) of the emitter. As a matter of fact, this type of emitter with these parameters is used in our laboratory for steady-state experiments.

The last type of semiconductors emitter takes advantage of the surface depletion field which acts as an accelerating field for photoexcited electrons instead of bias voltage. Such an electric field is perpendicular to the emitter surface and the emitted THz field vanishes for the normal incidence of the excitation optical beam. Arrangements with oblique incidence (e.g. near the Brewster angle) are then required. These emitters are also often placed into a magnetic field in order to enhance the emitted THz power. A typical example of materials of this group are InAs [9] crystals or semi-insulating GaAs crystals [10].

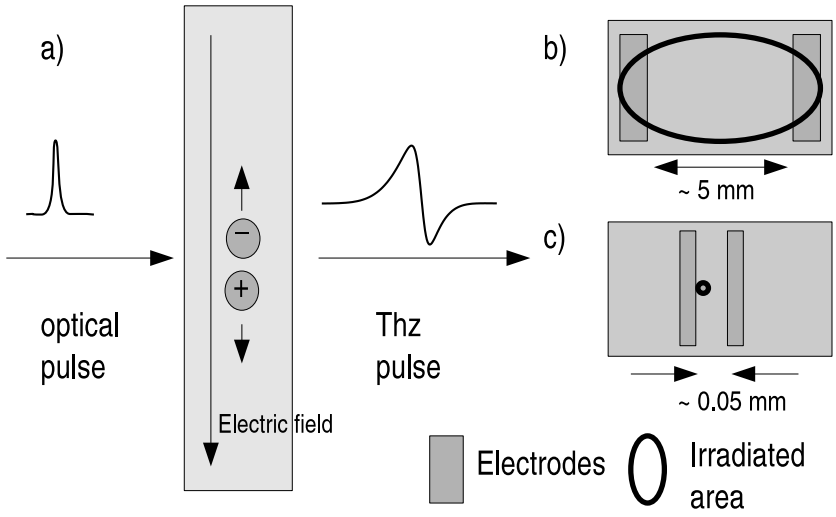

Figure 1.2: (a) Illustration of THz generation by photoconductive antenna. (b) Scheme of large aperture antenna (c) Small aperture antenna

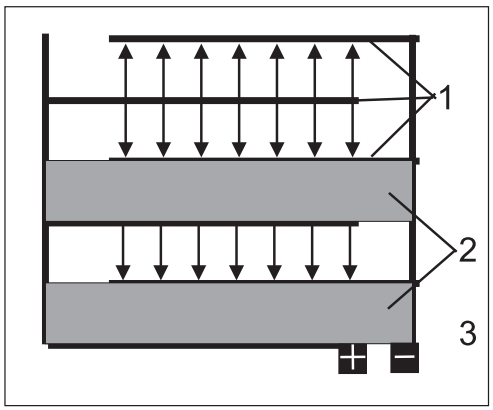

Figure 1.3: A scheme of MSM THz emitter: 1. Metallic finger-like integrated electrodes; 2. opaque metallization shadowing one electric field direction 3. SI GaAs substrate. Arrows represent direction of the electric field.

1.2.2 Optical rectification

Optical rectification (OR) is a second-order nonlinear optical effect, which takes place in noncentrosymetric materials. It can be easily explained as a three-wave mixing process of difference frequency generation [11] with close frequencies ν_1 and ν_2 creating a terahertz photon with frequency $f = \mid \nu_1 - \nu_2 \mid$. In the case of the generation of THz radiation, ultrashort femtosecond pulses are used as source radiation while the frequency mixing occurs between frequencies within the optical pulse bandwidth. This bandwidth is increased when shorter pulses are used. Thus more distant frequencies can mix and the THz pulse spectrum may broaden.

The intensity of the generated THz field depends on the intensity of the excitation pulse, the nonlinear coefficient of the second-order susceptibility and the phase matching condition. As OR is a second-order nonlinear process the intensity of optically rectified THz signal is proportional to the square of the pump pulse intensity.

THz generation via OR can occur in various materials, therefore it is necessary to distinguish between the particular mechanisms of the generation. If the energy of the photons is higher than the band-gap energy of the non-linear material, free carriers are generated and, the nonlinear susceptibility coefficient achieves a high value due to a resonant enhancement. This type of OR leads to the THz generation in materials like polar semiconductors, namely GaAs [12], [13] or CdTe [14] at 800 nm excitation (with Ti: sapphire lasers).

Otherwise, in the case when the photon energy is smaller than the band-gap energy, the carriers are only displaced in an anharmonic potential (virtual transition) and the fulfillment of the phase-matching condition becomes very important. This condition is

usually characterized by the pulse walk-off defined as a difference between the group refractive index of the optical pulse $n_{\mathrm{g,opt}}$ and the refractive index at THz frequencies N_{THz}. The typical example of materials where the transition is nonresonant and the walk-off condition nearly vanishes for an excitation close to 800 nm is ZnTe [15]. In this material, the efficiency of OR is limited by the process of two-photon absorption, which is not negligible at high pump intensities. This method with a ZnTe emitter is also used in our laboratory. Using 50 fs pulses with 0.2 mJ pulse energy and 810 nm mean wavelength, a THz pulse with the maximum electric field $\sim$ 5 kV/cm can be generated in a 1 mm thick ZnTe emitter. The spectral range of the generated THz pulse spreads from 0.1 GHz up to 3 THz, while at higher frequencies near 5.3 THz the radiation is absorbed in ZnTe due to a TO phonon.

Another representative of this group of materials is 4-N,N-dimethylamino-4'-N'-methyl stilbazolium tosylate (DAST) or 2-methyl-4-nitroaniline (MNA). These materials are transparent organic molecular crystals which are composed of molecules with very high electronic polarizabilities, implying high nonlinear coefficients. As these nonlinearities have a purely electronic origin without any vibronic contribution, the relevant nonlinear coefficient responsible for optical rectification is huge compared to inorganic crystals.

An advantage of the DAST organic salt is that it can be used in an experimental setup driven by a telecommunication-wavelength 1.5 μm laser. In such a setup a continuous spectrum ranging from 1.3 to 4.8 THz with a very high conversion efficiency ($E_{\mathrm{THz,max}} \sim$ 50 kV/cm at the optical pump-pulse energy of 25 μJ in a 0.6 mm thick crystal) was reported [16]. Moreover, ultrafast fibre lasers have only small dimensions in comparison to Ti:sapphire lasers, which may lead in the near future to spectroscopic THz setups fitting into a briefcase.

The phase-matching condition is fulfilled only in a few specific materials. In general, the THz refractive index N_{THz} happens to be larger than the optical refractive index $n_{\mathrm{g,opt}}$ due to the dispersion in the infrared range. However, even in this case THz radiation can be generated using so a called Cerenkov-like emission method, which will be discussed in the following Section.

Finally, in centrosymetric materials such as metals [17] or in $\langle 100 \rangle$-oriented InP [18], the presence of the surface depletion field induces the quadratic electrooptic effect and the whole process can be described as a four-wave mixing.

1.2.3 Cerenkov-like emission of THz radiation

Historically, Cerenkov radiation was observed as blue light coming out of water surrounding nuclear reactors. It is caused by a charged particle traveling through an insulator with a speed higher than the speed of light in that medium. The velocity that must be exceeded is the phase velocity rather than the group velocity. The traveling charged particle disturbs the local electromagnetic field in the medium and the medium becomes polarized. After the disruption passes away the insulator restores its equilibrium by emitting photons. In

the case of a particle traveling faster than light propagating through the medium, the excited atoms emit the light in the form of coherent radiation on a characteristic cone. In far field, the radiation constructively interferes, which intensifies the observed wave (see Fig. 1.4).

A similar principle can be used in order to generate THz radiation. By the propagation of ultrashort laser pulses in a medium lacking the inversion symmetry a second-order nonlinear polarization at THz frequencies is induced. This nonlinear polarization moves along with the laser pulse with speed $c/n_{\mathrm{g,opt}}$ and plays the role of the particle propagating with the super-luminar speed (i.e. super-luminar with respect to THz radiation, as $c/N_{\mathrm{THz}} < c/n_{\mathrm{g,opt}}$). The Cerenkov cone of pulsed radiation with a duration of approximately one cycle can be observed. The cone angle is given by the ratio of THz radiation velocity to the group velocity of the optical pulse. In contrast to classical Cerenkov radiation, where the material is excited by a point charge of a particle, the charge state of the effective source is neutral (the dipole moment). This radiation was for the first time observed in Lithium tantalate [19]. In that case the maximum THz field of 10 kV/cm was produced using femtosecond dye laser with 0.1 nJ energy in pulse.

This type of radiation can also be observed in centrosymetric media such as gases. In that case it can be described as a third-order nonlinear four-wave mixing process. Three types of experiments can be found.

1. Using a femtosecond laser, pulses of fundamental and second-harmonic frequency (created in second harmonic generation crystal) are focused to peak intensities higher than 10^{14} W/cm^2 in air. Because of the multiphoton absorption the air is ionized and coherent

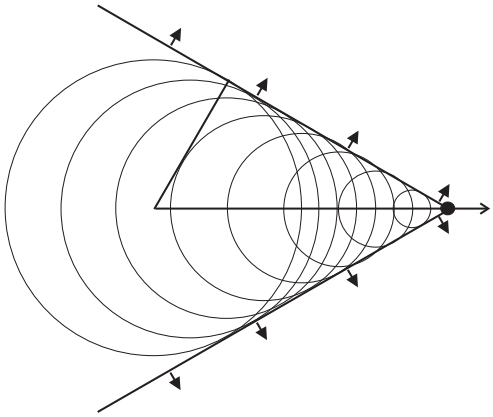

Figure 1.4: A schematic sketch of Cerenkov-like radiation. A particle traveling through dielectrics induces polarization of material. Photons emitted by depolarization constructively interfere in the far field if the speed of the particle is higher than the speed of light in the dielectrics. Characteristic Cerenkov cone of coherent radiation is created.

THz radiation of units of kV/cm can be created [20, 21]. An improvement of the intensity of THz radiation can be achieved when air is exchanged with noble gases [22] which are placed in gas chamber under the pressure of 700 torr. The highest THz emission of 21.7 kV/cm was observed in Xe with the incident fundamental beam energy of 650 μJ.

2. A generation of second harmonic which causes the experimental setup to be difficult to adjust can be avoided if the gas is ionized in the space between two electrodes with applied bias using amplified femtosecond pulses with the pulse energy of ≈500 μJ. If the electrodes are separated by a 0.8 mm distance and biased with 10 kV/cm, THz radiation at frequencies 0.2 - 2.5 THz can be observed [23].

3. By focusing intens femtosecond pulses to an area with the diameter of tens of micrometers stable plasma filaments with typical lengths in units or tens of cm can be produced [24]. The filament stability is a result of the balance between the self-focusing of femtosecond laser pulses due to optical Kerr effect and the diffraction effect. The source of Cerenkov-like radiation is an electric current moving in the plasma channel behind the ionizing laser pulse where the length of the filament defines the emission angle (i.e. donut-like spatial profile is generated). The filaments can be created in air in distant places (up to hundreds of meters from the laser source), the propagation length of the THz beam in the atmosphere then can be minimized. However, the energy for the creation of the filament is rather high (4 mJ).

1.2.4 Tunable THz-wave parametric generation

A tunable THz-wave parametric generation (TPG) is based on a phase-matched THz generation in nonlinear optical crystals (in $LiNbO_3$ [25] MgO:$LiNbO_3$ [26] or $LiTaO_3$). A typical experimental setup is shown in Fig. 1.5. An intens IR pulsed laser with relatively high spatial coherence (typically Q-switched Nd:YAG) pumps the nonlinear crystal where a simultaneous generation of a THz and an idler wave occurs. The nonlinear crystal is placed in the idler-resonator, where the pump beam and the idler beam form a small angle ($\approx 1^\circ$). The resonator mirrors are half-coated so that the pump beam propagates trough an uncoated area without scattering and the idler beam is reflected to set up the resonator feedback (see Fig 1.5.I.). THz radiation is created in polar crystals like $LiNbO_3$ or $LiTaO_3$ with a length of a few centimeters under strong illumination. In order to couple out THz radiation efficiently to the free space a grating structure on the surface of the nonlinear crystal or a prism coupler can be used. Due to the non-collinear parametric generation a wide tunability can be accomplished simply by changing the angle between the incident pump beam and the resonator axis. The tuning range of parametric generators is limited either by the restrictions on phase matching, or by the transparency region of the nonlinear material, or by the spectral region with high reflectivity of the resonator mirrors.

To conclude, by using the output of a Nd:YAG laser with a 1.5 mm beam diameter and 25 ns long pulses, with an energy of 30 mJ/pulse a continuously tunable THz radiation in the 1-3 THz range can be obtained with the spectral resolution of 10 GHz. THz pulses are

10 ps long have the energy of 192 pJ/pulse ($\approx$ 20 W at the peak) and the system operates at room temperature [25].

An effective TPG can be also built without the idler resonator cavity. A so called injection-seeded THz parametric generator (IS-TPG) is equipped with a fibre laser or an external-cavity diode laser as an injection-seeder for the idler [27](see Fig 1.5.II.). The tunability of the system (0.7 to 2.4 THz) can be achieved by a change of the seed wavelength and a simultaneous adjustment of the seed incidence angle. The single-pass nature of the system makes it rugged and greatly simplifies wavelength tuning, because no cavity-locking mechanisms are needed. Moreover, the peak THz output power in IS-TPG reaches the values of 250 W (900 pJ/pulse) and the spectral resolution is of 100 MHz. In this case the THz pulses are 3.4 ps long.

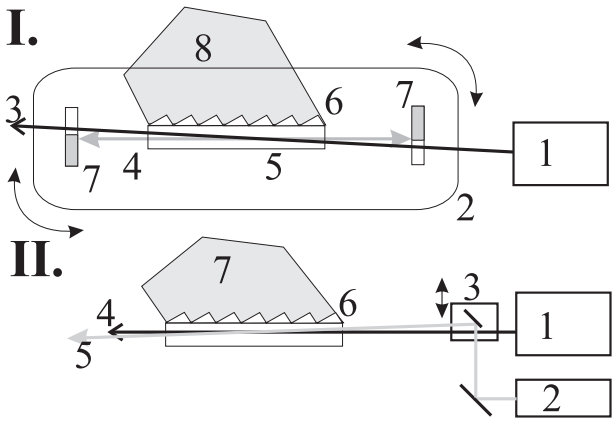

Figure 1.5: I. Scheme of a tunable THz parametric oscillator: 1 Q-switched Nd:YAG laser, 2 rotary stage 3 pump beam, 4 idler beam, 5 $LiNbO_3$ crystal, 6 Si prism, 7 half-coated mirrors, 8 THz radiation; II. A scheme of tunable THz generator: 1 Q-switched Nd:YAG laser, 2 tunable continuous-wave laser diode (seed), 3 mirror on a y-stage, 4 pump beam, 5 idler beam, 6 Si-prisms, 7 THz radiation.

1.2.5 Quantum cascade lasers

Quantum cascade lasers (QCL) are semiconductor laser devices that are capable of producing monochromatic coherent radiation ranging from mid-infrared to terahertz frequencies. Unlike typical interband semiconductor lasers that emit electromagnetic radiation through the recombination of electron-hole pairs across the material band gap (the longest wavelength lead-salt classical laser diodes do not reach frequencies below 15 THz), QCLs are unipolar and laser emission is achieved through the use of intersubband transitions in a repeated stack of semiconductor superlattices.

A QCL is composed of a periodic series of semiconductor thin layers like GaAs and Al_xGaAs_{x-1}, prepared by molecular beam epitaxy, forming a superlattice. The one-dimensional multiple quantum-well confinement leads to the splitting of the conduction band of permitted energies into a number of discrete electronic subbands. By a suitable design of the layer thicknesses it is possible to engineer a periodically repeated active region (with discrete electronic levels) and injector region (with electronic subbands). When a bias voltage is applied on such a structure the energy levels of subbands neighboring the active region shift to allow injection of electrons to the upper lasing level and efficient depopulation of the lower lasing level. This makes possible to achieve the population inversion in the active region. Electron transported through the active area emits the difference energy as a low-energy photon. Subsequently, the electron is injected into the next active region which results in the creation of typically 25 to 75 photons per single electron cascade transit. Since the positions of the energy levels in the system are primarily determined by the layer thicknesses and not by the material, it is possible to tune the emission wavelength of QCLs over a wide range in the same-material system by the structure design. In a QCL, the mentioned quantum well structure is embedded in a waveguide, and the laser resonator feedback is usually ensured by Distributed Bragg reflectors.

Historically the first QCL was developed in 1994 [28]. However, its lasing frequency was about 75 THz. The lasing at 4.4 THz was demonstrated in 2002 [29] at the maximum operating temperature of 50 K, but only with 120 μW of peak output power with 100 ns long pulses.

QCL can work both in pulsed or continuous regime. The continuous emission is usually achieved at lower temperatures. The maximum temperature operation still remains very low for the QCLs operating in the THz range. Although there is no fundamental physical reason, it follows from the recent experiments that with current designs of QCLs the inequality $h\nu \gtrsim k_bT$ roughly holds (ν is the laser frequency and T is the operation temperature) [30]. This confines the operation temperature to $T \lesssim 50$ K for 1 THz. The QCLs development thus becomes more challenging towards lower frequencies. This is because of the depopulation of carrier inversion in the active region, which is caused by thermal heating. For example at the lasing frequency of 1.2 THz the maximum working frequency drops down to 84 K for a pulsed operation and to 10 K for a CW operation [31]. At 3 THz the maximum working temperature was reported to be 178 K for a pulsed regime [32]

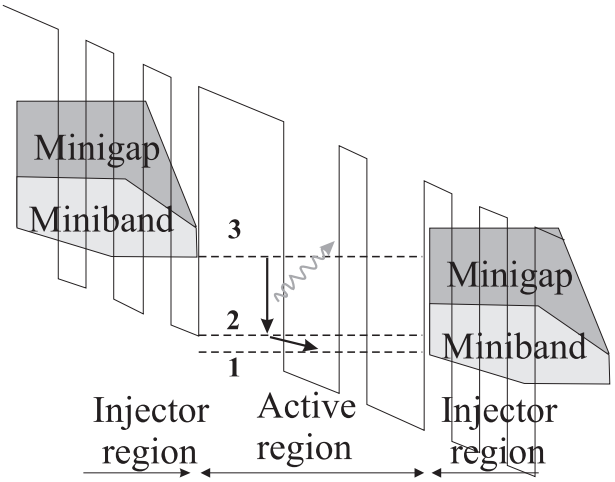

Figure 1.6: I. Schematic diagram of the conduction band structure of the quantum cascade laser. A THz photon with frequency $\nu = (E_3\text{-}E_2)/h$ is generated.

and 117 K for a continuous regime [33]. The room temperature operation can be achieved only for much higher frequencies (for example 34 THz [34]).

The average output power of QCLs dramatically increases with decreasing temperature. While at maximum working temperature the maximum average output power reaches hundreds of microwats (for pulses typically 200 ns long), the output at very low temperatures typically rises to hundreds of milliwats. For example, 248 mW peak power in the pulsed mode, and 138 mW continuous-wave power outputs at the temperatures of 10 K at 4.4 THz frequency was reported [35].

On the other hand, the QCLs working at mid-infrared frequencies are much less complicated, easier to built and they are capable of producing CW radiation at room temperatures. (output power of 1.5 W at 65 THz [36]). Another approach to the generation of longer wavelengths seems to be in their combination with a frequency down-conversion in nonlinear optical crystals with giant second-order nonlinear susceptibility [37]. It was demonstrated that in a dual-wavelength QCL laser with the working frequencies of 33.7 THz and 28.5 THz with the active region engineered to possess a giant second-order nonlinear susceptibility associated with intersubband transitions in coupled quantum wells, THz radiation at 5 THz with the conversion efficiency of 5 μW W^{-2} can be generated (at 80 K the device had output of 7μW). However, at the room temperature the output peak power of the difference frequency was only in order of hundreds of nW for 60 ns long pulses at a 250 kHz repetition rate [38].

1.2.6 Backward wave oscillators

A backward-wave oscillator (BWO), also called carcinotron, is historically one of the oldest THz sources (1960s). It produces continuous-wave THz radiation approximately in the range from 30 GHz to 1.4 THz [39]. It is a tunable source of high-power (up to 300 mW at low frequencies and 1 mW at high frequencies) and highly monochromatic ($\Delta f/f \approx 10^{-6}$) radiation.

The BWO (see Fig.1.7) is a similar device to the conventional electrovacuum diode and triode. A cathode heated up to 1200 °C serves as the source of the electrons. In vacuum electrons are collimated by an external permanent magnet and accelerated towards the anode using high voltage (up to 6 kV); current densities of up to 150 A/cm^2 are reached. During their path the electrons travel through a comb-like fine-structure electrode slowing system, which transfers their kinetic energy to the THz electromagnetic field. By moving in the periodic potential of the slowing system, the electrons are grouped periodically in bunches and produce an electromagnetic wave traveling in the opposite direction to the electrons (backward wave). The tuning of the THz emission is realized by adjusting the high voltage and by a replacement of the BWO source, where each BWO source can be continuously tuned within 200 GHz range.

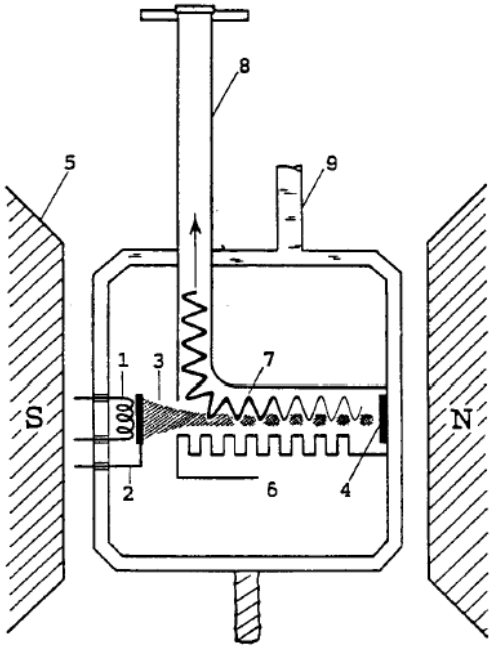

Figure 1.7: Schematic diagram of a BWO: 1 heater, 2 cathode, 3 electron beam, 4 anode (collector), 5 permanent magnet, 6 comb-like electrode, 7 electromagnetic wave, 8 waveguide, 9 cooling water. (From Ref. [40].)

1.2.7 Free electron lasers and synchrotrons

A synchrotron and a free electron laser, or FEL, are sources of high power coherent electromagnetic radiation. Unlike gas, liquid, or solid-state lasers, in which electrons are excited in bound atomic or molecular states, synchrotrons and FELs use a relativistic electron beam as the lasing medium, which moves freely through a magnetic structure.

The coherent synchrotron radiation is in FELs created in undulators or "wigglers" where electrons accelerated to relativistic speed are forced to assume a sinusoidal path due to interaction with a periodic transverse magnetic field (see Fig. 1.8). Electrons which are forced to accelerate or decelerate emit intense radiation. The acceleration and deceleration of electrons is in phase with the emitted light so the fields add coherently. The wavelength of the emitted light can be readily tuned by adjusting the energy of the electron beam or the magnetic field strength of the undulator. In synchrotrons the radiation is generated in places where the electrons are forced to change their direction.

The largest difference between FELs and synchrotrons is in the principle of accelerating the electrons to relativistic energies, however, the principle of emitted radiation is the same. While in FELs linear accelerators are used, in synchrotrons the electrons are accelerated in cyclic accelerators. Both FELs and synchrotrons are complicated apparatuses which are known of producing intense THz radiation. However, originally the FEL was created to primary produce not THz but IR radiation. In the case of synchrotrons, the target radiation was X-rays. THz radiation was observed as a side effect which is now intensely used.

Pulsed coherent THz radiation generated from electron bunches in synchrotrons can reach a peak pulse power up to 2.4 W and an average power up to 1 mW in the range from 0.4 to 1.5 THz [41]. The observed pulses were 3 ps long, they were created by 100 electron bunches with the circling synchrotron frequency of 1.8 kHz. The average spectral power density was found to be 0.2 Wcm.

Similar average power density was reported from a FEL facility [42], where the electron bunches, which were 500 fs long, were accelerated to 40 MeV energy with repetition rate of 75 MHz.

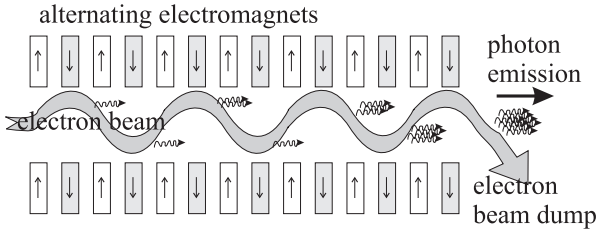

Figure 1.8: Schematic sketch of an undulator. Electrons which feel presence of alternative magnetic field emit coherent radiation.

1.2.8 Coherent THz Radiation from Superconductors

Recently a novel approach to generate coherent THz radiation based on a high temperature superconductor $Bi_2Sr_2CaCu_2O_8$ (BSCCO) has been presented [43]. Coherent continuous-wave THz radiation is generated in stacks of so-called Josephson junctions that exhibit a unique electrical property: when an external DC voltage is applied, an alternating current will flow back and forth across the junctions at a frequency proportional to the strength of the voltage; this phenomenon is known as the Josephson effect.

A single Josephson junction, consisting of two superconducting electrodes separated by a thin insulating layer, is a relatively weak source of radiation. It naturally converts DC voltage into THz radiation (0.36-0.85 THz), where the frequency of radiation is given by the junction width and refractive index. In a Mesa BSCCO structure more than 500 junctions can work with a synchronized phase of the emission. The synchronization is achieved due to the creation of a standing electromagnetic wave inside the BSCCO crystal, which represents a cavity analogous to the laser. The emission power was found to increase as the square of the number of junctions reaching values of 0.5 μW at frequencies up to 0.85 THz, and persisted up to ≈50 K.

1.2.9 Terahertz radiation from shocked materials

Lately, narrow-band coherent electromagnetic radiation in the frequency range of 1-100 THz has been theoretically predicted from crystalline polarizable materials like NaCl when they were subjected to a compressive shock wave producing a small strain of typically ≈1% [44]. The radiation is generated by an oscillating material polarization resulting from the synchronized nonresonant motion of a large number of atoms induced in the nonequilibrium region at the front of a planar shock wave propagating through the crystalline lattice. The frequency of the generated radiation is associated with the velocity at which the shock propagates through the lattice planes and, therefore can potentially be used to determine atomic-scale properties of the shocked material. It has been proposed that specifically shaped wave front of the shock wave can lead to a highly directional THz emission.

1.3 THz detectors

There are two most common types of the detection of THz radiation. The first one, which will be in this section represented by bolometer technique is based on the absorption of the THz electromagnetic field. The absorbed radiation heats the detector and the change in the temperature is subsequently detected typically as a change of the voltage. This type of detectors is commonly used with monochromatic THz sources where it provides an information about the intensity $I =\mid E(f) \mid^2$ and not about the phase of the radiation.

The second type of detection is primarily used in spectroscopic measurements with ultrashort THz pulses (time-domain THz spectroscopy). Its main advantage is that it can be phase sensitive. It means that one can access here both the amplitude and the phase of any frequency component of a broadband THz pulse. The method allows one to reconstruct the time-domain waveform of the THz electric field and, after the Fourier transformation, a complex broadband response function can be obtained from a single measurement without using the Kramers-Kronig relations. Methods allowing this kind of detection like photoconductive gating, electrooptic (magnetooptic) sampling or THz-induced lensing profit from the time synchronization of the THz pulses with femtosecond laser pulses which are typically used within the same experimental setup for the THz generation.

The shape of the THz waveform is typically reconstructed by a sampling technique triggered by gating pulses (split from the output laser pulse train), where the detection signal depends on the instantaneous THz field overlapping with gating pulse. By changing the arrival time of the gating pulse, the field of the entire THz pulse (THz waveform) can be scanned.

The measured THz waveform E_{meas} practically always differs from the true one E_{true}. The difference can be caused by several effects (e.q. optical and THz pulse walk-off in the sensor, finite length of the optical pulse etc.) and it can be described by the response function of the detector D. In frequency domain the relation between the measured and true electric fields reads:

$$E_{\mathrm{meas}}(f) = E_{\mathrm{true}}(f).D(f) \tag{1.1}$$

Fortunately, for steady-state (equilibrium) spectroscopic measurements (Section 2.3.1) the detector response function is not necessary for the data processing. However, in more advanced experiments like ultrafast pump-probe schemes (Section 2.3.2) its knowledge is essential.

1.3.1 Photoconductive receiving antennas

A way to detect THz radiation using a photoconductive antenna is practically inverse to the way of generating THz radiation explained in Section 1.2.1. The incident (sampling) pulse generates free carriers in the gap between electrodes of photoconductive dipole antenna in a semiconductor film or wafer. The length of the ultrashort sampling pulse gives the resolution of the sampling process. Photogenerated carriers are during their lifetime accelerated in the presence of the THz field. They generate a current which is converted to a voltage by a current amplifier connected to the feed lines of the antenna (see Fig. 1.9. The photoconductivity response is the limiting factor to the upper-most frequency of such antenna structures. The photocurrent J can be calculated as a product of the transient photoconductivity σ and the THz electric field E across the photoconductor: $J(\omega) = \sigma(\omega)E(\omega)$ in the frequency domain and as a convolution $J(t) = \sigma(t) * E(t)$ in the

time domain. In order to make $E(t)$ approximately proportional to $J(t)$ the photoconductivity response has to be much shorter than the THz waveform (in other words $\sigma(\omega)$ has to be flat function of ω). To reach this goal the lifetime of generated free carriers needs to be short (in the range of hundreds of femtoseconds). Ideal materials achieving this properties are RD-SOS and LT-GaAs. However, LT-GaAs is usually preferred due to its higher carrier mobility, which leads to a stronger signal.

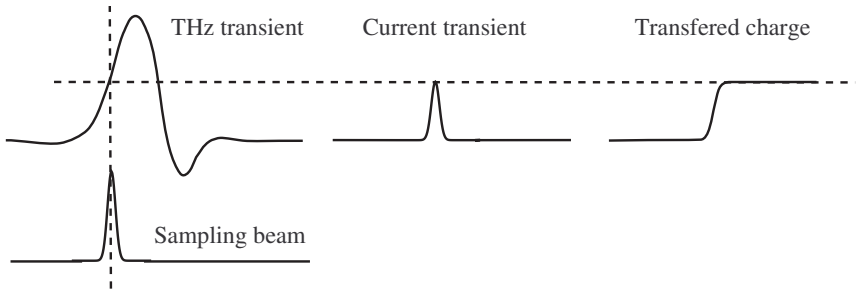

Figure 1.9: Scheme of photoswitch sampling technique: Ultrashort pulse generates in semiconductor photocarriers which are accelerated in the presence of THz electric field. The total charge transferred during one pulse is proportional to the amplitude of THz beam at the moment of the sampling pulse arrival.

On the other hand, the detection using carriers with long lifetime is also possible (for example in semi-insulating GaAs or Si). The drawback is that only the primitive function of the THz field $\int_{-\infty}^{t} E(t')dt'$ is detected by the detector and thus a differenciation needs to be performed. As a consequence, the detection sensitivity is proportional to the reciprocal frequency for higher frequencies. Photoconductive antenna sensitive up to 20 THz based on low-temperature grown GaAs with a carrier lifetime of 1.4 ps and using 15 fs gating pulses was reported [45].

1.3.2 Electrooptic sampling

Electrooptic sampling is a detection method based on the linear electrooptic Pockels effect. In classical Pockels effect a birefringence of an electrooptic crystal is induced by an applied voltage. In our case the role of the applied voltage is played by the THz field E_{THz} (Fig. 1.10). Let assume a simplified case, when the phase matching condition for the THz and optical pulse is fulfilled. In the electrooptic crystal during the presence of the THz pulse the birefringence at optical frequencies linearly follows the shape of the THz pulse:

$$\Delta n \propto E_{\mathrm{THz}}; \tag{1.2}$$

in this way, the change in the polarization state of the optical ultrashort sampling pulse can be used to evaluate the instantaneous THz field (given the delay between the two pulses).

In a crystal with thickness L the phase shift between the ordinary and extraordinary part of the sampling beam is

$$\Delta\varphi = \frac{\omega}{c}\Delta n L. \tag{1.3}$$

This phase shift is responsible for a slight change in polarization of the initially linearly polarized optical pulse into slightly elliptical. To transfer the polarization to almost circular a $\lambda/4$ plate is used. Subsequently, the horizontally and vertically polarized parts are separated by a Wollaston prism; their intensities are measured by a pair of balanced antiparallel photodiodes. The difference between these intensities equals:

$$\Delta I = I_0 \Delta\varphi \tag{1.4}$$

where I_0 is the intensity of the sampling beam. For sufficiently small values of $\Delta\varphi$ the measured signal is directly proportional to E_{THz} (one obtains for 1 mm thick ZnTe crystal and for fields below 10 kV/cm the linearity with a precision better than 1%).

To reliably detected the difference signal ΔI_0 with a lock-in amplifier the THz electric field is modulated. This is typically done with a chopper placed before a THz emitter. In amplified femtosecond laser system with the repetition rate of the femtosecond pulses of 1 kHz an additional improvement in the detection can be achieved using time-selective amplification by a box-car averager (gated integrator). The signal-to-noise ratio of the

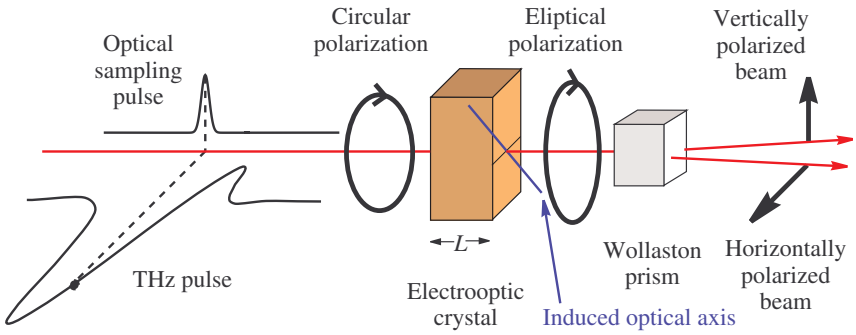

Figure 1.10: Principle of electrooptic sampling: Circularly polarized optical ultrashort pulse changes its polarization state in the electrooptic crystal in presence of much longer THz pulse. Wollaston prism spatially separates the horizontally and vertically polarized outgoing beams; the difference in their intensities (proportional to the sampled THz field) is directly detected by pair of balanced antiparallel photodiodes.

detected electric field THz-waveform can be obtained to be higher than 10000:1 in this case.

Similarly as in the nonlinear crystals for the generation of THz radiation, the phase matching condition has to be considered. Unfortunately, it is rarely possible to achieve the phase-matching condition for the whole bandwidth of the THz pulse. For ZnTe, the phase-matching condition is quite well satisfied for frequencies below 2 THz if sampling pulse at 800 nm is used [46]. In ZnTe the upper detectable frequency range is limited by the absorption of the TO-phonon resonance at 5.3 THz. Practically, the ZnTe detector is used for efficient detection of frequencies below 3 THz. For higher frequencies, materials such as GaAs [46] and GaP [47] constitute a more suitable choice.

1.3.3 Magnetooptic sampling

For the detection of THz radiation the magnetooptic properties of materials such as terbium-gallium-garnet and amorphous glass SF-59 [48] can also be used. Magnetooptic sampling is based on the Faraday effect, where in the presence of the magnetic field (in our case the magnetic component of the THz wave) the index of refraction in the magneto-optic sensor is modulated. The experimental setup requires orthogonal geometry (Fig. 1.11), as the magnetic field needs to be parallel with the sampling-beam propagation direction. The sensitivity of 10^{-7} T can be achieved. The rest of the experimental setup, including the Wollaston prism and a pair of balanced antiparallel photodiodes, is the same as in the electrooptic sampling detection scheme.

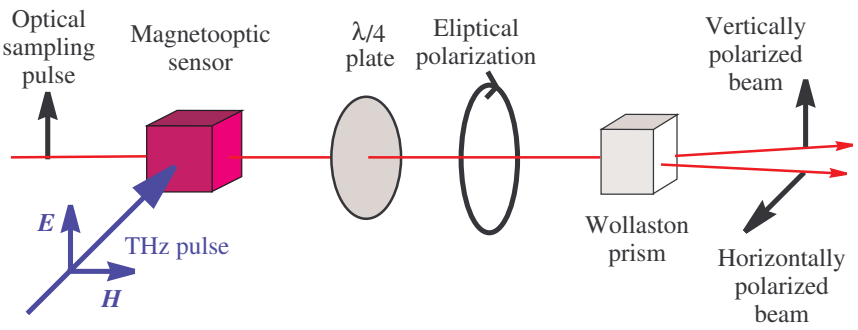

Figure 1.11: Scheme of the free-space magnetooptic sampling technique.

1.3.4 Terahertz-induced lensing

Recently a novel method for the detection of THz radiation has been presented [49]. In electrooptic crystals the focusing and defocusing of the sampling laser pulse is induced by

the collinearly traveling THz pulse. At a given distance behind the electrooptic crystal the on-axis intensity of the ultrashort sampling pulse changes linearly with the THz electric field. In materials commonly used for THz detection like ZnTe or GaAs the sensitivity of the THz induced lensing (TIL) is four times lower than the sensitivity of the standard electrooptic sampling.

In contrast, for DAST the detection using TIL is advantageous and its sensitivity even exceed that achieved in a standard electrooptic setup. This is due to its very large EO coefficients which can be in this type of geometry effectively used. On the other hand, DAST exhibits strong birefringency (it has a monoclinic crystal symmetry) which prevents for its use in the standard EO sampling.

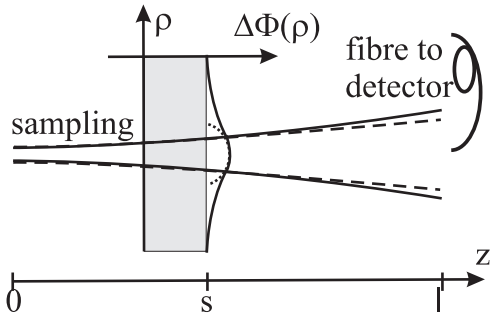

Figure 1.12: Scheme of the THz-induced lensing: Sampling beam is focused by THz-induced phase shift $\Delta\Phi(\rho)$ creating a plano-convex lens (dotted line). Solid/dashed line represents the probe beam without/with presence of the THz field. s indicates the position of electro optic crystal, while l indicates the position of the optical fibre which guides the signal to the detector.

1.3.5 Bolometers

Bolometers are devices for the detection of any kind of radiation. However, in the far-infrared region of the electromagnetic spectrum they represent the best choice owning to their high sensitivity. Technically, they are thermometers - they detect the power of incoming radiation by registering the resulting rise in temperature due to absorption. More specifically, a bolometer detector consists of an extremely thin superconductor foil, for example niobium nitride, where a slight change in the temperature of the foil is observed as a measurable change in its resistance which is subsequently transformed to the output voltage. The need to measure small temperature fluctuations requires the bolometers to be cooled down to liquid helium temperatures.

Bolometers are often used by astronomers to detect radiation coming from outer space or they can be used in laboratories for the detection of IR signal in FTIR spectrometers in

interferometric setups. The interferograms of THz pulses provide only the THz transient amplitude spectrum, however, they do not give the information about the phase. This does not allow the reconstruction of the pulse shape in the time domain. Nevertheless, the information about the phase can be obtained if the sample is placed into one arm of the interferometer. For this purpose a Mach-Zehnder interferometer is usually used with BWO as a source of tunable monochromatic THz radiation; here during the frequency scan, the position of the mirror in the empty arm of the interferometer is continuously adjusted by the computer-feedback system in order to sustain the interferometer in balanced state (zero signal on the detector). The measured quantity in this case is the mirror displacement. In other words, the spectrometer registers the change in the optical thickness of the sample vs. frequency.

1.4 THz applications

Over the past decade, there has been a staggering increase in the number of research groups worldwide seeking to develop and exploit the terahertz frequency range. The fruits of this research can be seen in different domains of physics [50, 51], medicine [52] or security [53, 54]. These applications sit alongside the traditional needs for terahertz sources and detectors (LT-GaAs, InP, InGaAs, DAST, Au-film and others), systems for current and future astronomical programmes, as well as for studies of condensed-matter physics (semiconductors: doping, scattering of free carriers, dynamics of photoexcited carriers; superconductors; metamaterials: negative refractive index; ferroelectrics and magnetoelectrics : polar phonons and relaxational mechanisms responsible for phase transitions), biology (spectral fingerprints of molecules such as explosives or drugs) and nanoscale structures, for which the key-energy scales lie in the terahertz spectral range.

For example astronomers use THz radiation to detect presence of molecules, mainly the water molecule, in the outer space due to their absorption. Another applications based on strong absorption of THz radiation in water can be found in biomedical research. For example it is known that cancerous tissue has higher water content than the healthy tissue thus it could be used for an early detection of skin cancer [55], [56]. THz reflection imaging techniques are capable of the detection of tumors, namely skin tumors which are not visible to the naked eye because they are buried under the top layer of the the skin.

Dental Caries, or tooth decay, is one of the most common human disorders. A localized destruction of the enamel (outside layer of the tooth) is an initial cause of caries. Healthy enamel can be distinguished from carious enamel by lower attenuation of the THz signal [57, 58]. With this special abilities THz imaging can make dental care more concentrated to prevention and stop the caries long before dentist's painful procedures.

Many unique properties of THz radiation (plastics, wood, textile, ceramics are transparent in the THz range; water strongly absorbs THz radiation; metallic surfaces reflect THz radiatin) in combination with contact free detection make THz radiation ideal for

inspection of products. Although the outdoor THz setups are still being developed a few applications of products inspection are already commercially available. Production faults in flexible packages based on a large difference between the absorption coefficients of plastic and water or air and plastic in case of water- or air-filled channels (defects) of terahertz radiation was presented in [59].

Nondestructive terahertz pulse imaging is capable of characterizing the 3-D internal structure, the detection and identification of localized chemical or physical structure of pharmaceutical tablets [60].

The laser terahertz emission microscope was built to detect failures in the large scale integrated circuits [61]. The failures can be detected due to different THz emission from integrated chips compared to working ones.

One of the materials which is transparent for THz radiation is also plaster. Nowadays many frescos can lie forgotten or hidden under it. If there is a change in material through which the THz pulse propagates (plaster-painting) part of the signal is reflected back from the interface. Moreover, some colors contain metal particles, which increases the intensity of the reflected THz pulse [62].

Wood is an another THz transparent material. Its structure - long cellulose fibres created by the growth of a tree - can be visualized by THz imaging techniques [63]. The way how wood is structured, if it has the fibres aligned, twisted or cracked or if it is damaged by the pine beetle defines its quality and the price.

In this section a few of the applications, namely astronomical; narcotics, explosives and weapon detection and electrical integrated circuits inspection will be presented in more details.

1.4.1 Astronomy

A highly sophisticated bolometer cameras and other THz detectors are helping astronomers not only to observe the coldest parts of the universe, they also help them to trace a wide variety of chemical molecules. Because of the water absorption of THz radiation in the Earth's atmosphere, THz telescopes have to be located at the driest places, like deserts or high Antarctic plateaus (AST/RO, automated observatory Dome Argus), or as high as possible (Stratospheric Observatory for Infrared Astronomy SOPHIA, a 2.5 meter infrared airborne telescope in a Boeing 747-SP operating at above 12.5 km) or have to collect data from outer space (satellites: Herschel, ASTRO-F, Aura).

Generally, in millimeter and submillimeter region, molecules like OH, O_3, HCl, ClO, HOCl, BrO, HNO_3, N_2O, HCN, CH_3CN, volcanic SO, CO, CH_3OH, H_3O+, charged molecule composed of carbon and fluorine - the CF+ ion, hydrogen and deuterium (H2D+), water molecule and many others have their fingerprints and can be traced. Besides spectroscopic research of the universe the detected THz radiation is used to study formation of new stars from clumps in molecular clouds or other objects like galaxies at approximately -250 degrees Celsius temperature.

1.4.2 Electrical integrated circuits inspection

The demand for quality and reliability in integrated-circuit chips makes an inspection and failure analysis of large scale integrated (LSI) circuits very important. The laser terahertz emission microscope (LTEM) technique has recently joined other nondestructive methods for noncontact inspection of electrical failures in circuits [61]. The microscope is driven by a femtosecond laser which excites the LSI chips placed on a x-y movable table. With femtosecond pulses a transient photocurrent in the circuit is induced, which consequently give rises to THz radiation. The backward THz radiation is focused by a mirror to a LT-GaAs detector. The spatial resolution of LTEM system can achieve 3μm. By comparing the THz emission images of a normal and a damaged chip, the abnormal electrical field resulting from an electrical failure in the circuit can be visualized. However, because the multilevel interconnections in the case of multilayered structures in the chip prevent the generation and detection of the THz emission, a rear illumination through the substrate is necessary.

1.4.3 Narcotics inspection

Narcotics among many other chemical substances have characteristic frequency fingerprints in the THz range. When THz radiation passes through such a material a part of the radiation is absorbed; materials can be clearly identified from the absorption spectra according to the energy of specific intra- or inter-molecular vibrations.

Because of the lack of noninvasive techniques narcotics are often transported and distributed in envelopes or packages. In many countries officers are required to obtain a search warrant to examine the contents of the envelope or the package every time the need arises. If the narcotics are sealed in a plastic bag, without any traces of it on the envelope, the content of the bag can not be identified either by the X-rays (which can identify only the outline of a plastic bag or a tablet) or trained dogs.

A scanning device based on a THz parametric generator can be used to identify suspicious envelopes, as it was investigated in [26]. Illicit or legal drugs like methamphetamine or MDMA (DL-3,4-methylenedioxymetamphetamine) hidden in plastic bags in paper envelope could be recognized to a concentration of ≈20 mg/cm^2 by changing the wavelength of the emitted THz radiation in the frequency range from 1 to 2.5 THz. The TPO was driven by a Nd:YAG pump laser (wavelength 1.064 μm) and a nonlinear optical crystal MgO:$LiNbO_3$ (length 65mm). The signal was detected by a Si-bolometer. Although the system was capable of the isolation and extraction of spatial patterns of each component even in cases where the target was a mixture of multiple drugs or arranged in layers, the total time of the scans is of the order of minutes making this method useful only for detection of single-suspicious envelope rather than for a mass application.

1.4.4 Explosives and weapons detection

Similarly to narcotics, explosives are another group of chemical substances which can be detected via THz radiation [64], [65]. However, the detection of explosives is a more challenging task. For security applications, where a potential bomber needs to be detected within a certain distance, the propagation of THz radiation in the absorbing atmosphere plays a significant role.

The distance of the detectable propagation is limited by the water vapor absorption, which at 50% relative humidity at frequencies above 0.5 THz rises to between 0.1 and 10 dB m^{-1}. This, in turn, limits the stand-off distances when using greater than 0.5 THz frequencies for sensing and imaging the dielectric contrast of remote targets. However, high-brightness sources like BWOs, QCLs, femtosecond lasers or passive systems working with lower frequencies can bypass this problem.

The whole THz spectrum can be used for the identification of potentially dangerous materials or from the known reflection spectra of explosives [65] a few characteristic frequencies can be picked and the detection can be performed at these frequencies (for example RDX at 0.82 THz). A knife blade can be also easily detected because a metal surface reflects THz radiation well.

Products of companies like Picometrix (sensing of explosives in distance of 30 m), TeraView (Detection of explosives and ceramics weapons hidden in shoes), ThruVision (passive detection system T5000) or StarTiger (passive detection system at 0.2 - 0.3 THz) are nowadays commercially available. These systems are slowly shifting the THz security applications from the laboratory to airports and security posts.

Chapter 2

Time-domain THz spectroscopy

2.1 Introduction

In the past few decades the information technologies based on small and high-speed microelectronic devices changed almost all aspects of human life. These small semiconductor devices represent an endless challenge for innovations making them faster and more reliable. Their speed and dimensions are closely related, where in a transistor with a few tens of nanometers in length the electron transit time can be as short as a few hundreds of femtoseconds. The progress in this field is not possible without the basic understanding of various dynamical processes. The knowledge of these properties can be also exploited in many other fields of industrial and scientific applications (THz lasers, detectors, emitters...). Some of them were discussed in the previous chapter.

Time Domain THz spectroscopy is a well-suited method for semiconductor studies. It is a contact-free method able to follow the in-plane nanoscopic motion of charges with a sub-picosecond to nanosecond time resolution. In this chapter we will discuss different types of THz time domain spectroscopic methods and we will show how the properties of materials are measured, evaluated and modeled.

2.2 Experimental setup

The description of the experimental setup (shown in Fig. 2.1) needs to be started with the overview of our femtosecond laser system, which consists of the Coherent Mira Seed femtosecond oscillator (pumped by the Coherent Verdi pumping laser) and the Quantronix Odin multi-pass femtosecond pulse amplifier (pumped by the Quantronix Nd:YLF laser).

Verdi is a solid-state diode-pumped, frequency-doubled Nd: vanadate (Nd:YVO_4) laser with continuous-wave (CW) output power of 5.5 W at 532 nm, which is used to pump the Mira Seed femtosecond oscillator. The Mira Seed is a modelocked ultrafast laser oscillator that uses Titanium:sapphire (Ti:Al_2O_3) as a gain medium to produce ultrashort wide-

bandwidth pulses. The technique used to generate ultrashort pulses here is referred to as Kerr Lens Modelocking (KLM). Ti:Al_2O_3 shows an appreciable optical non-linearity. Because of the non-uniform lateral power density distribution in a Gaussian beam the refractive index experienced by the intracavity beam while traveling through the Ti:Al_2O_3 crystal is higher in its center than at its edges. This self-focusing phenomenon results in a higher round trip gain in the modelocked (high-peak power) versus CW (low-peak power) operation due to an increased overlap between the pumped gain profile and the intra cavity mode. Mira Seed laser generates 65 fs long pulses with the repetition rate of 76 MHz and energy per pulse 8 nJ at the wavelength of 800 nm. Its average output power is 650 mW.

The non-amplified system (consisting of Mira and Verdi) is in our laboratory used with a biased THz emitter described in Section 1.2.1 in steady state experiments. In order to study non-equilibrium processes in optical-pump THz-probe (OPTP) experiments, like the lifetime of the photoexcited carriers in semiconductors, the femtosecond pulses need to be amplified in the multipas femtosecond amplifier Odin which is pumped by an Nd:YLF laser.

The pumping YLF laser is an optically pumped (Krypton flashlamp) Q-switched laser, where the Q-switch is provided by an acousto-optic modulator and radio-frequency driver. Its IR pulses (1054 nm) are converted by means of an infra-cavity second-harmonic-generation (SGH) in a LiB_2O_3 (LBO) crystal into 527 nm radiation. The laser produces 10-ns-long pulses with 1.2 mJ pulse energy and repetition rate of 1 kHz. Its average output power is 12 W.

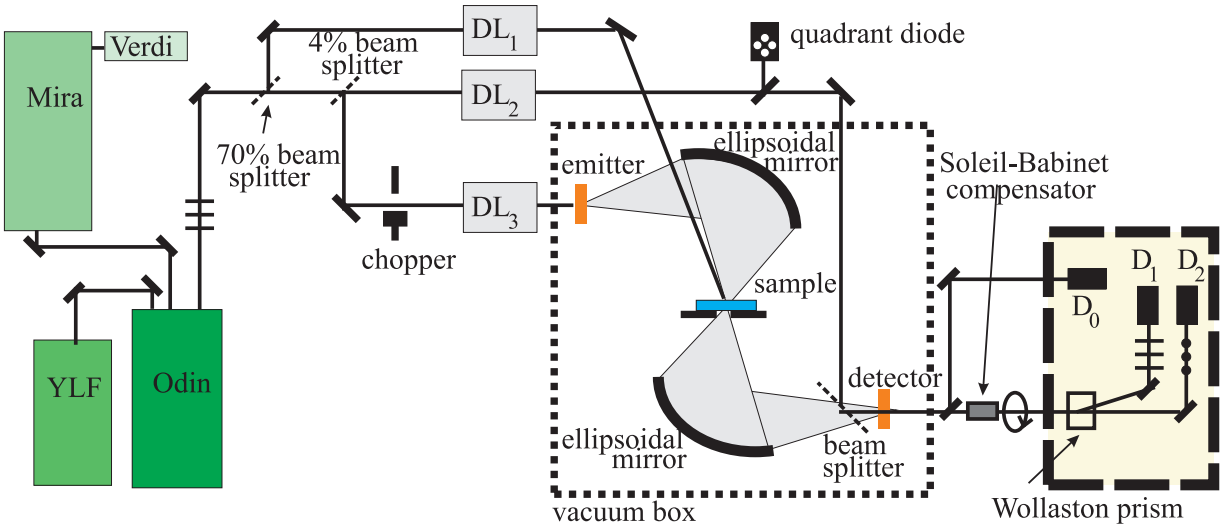

Figure 2.1: Scheme of the THz experimental setup.

In Odin, one in 76000 pulses provided by Mira Seed is picked by a Pockels cell. The pulse is first stretched to ≈ 30 ps. This is accomplished by means of a pair of gratings, where the red and blue portions of the spectrum travel via different optical paths through the stretcher. After the stretching process, the pulse passes 7 times through the Ti:Al_2O_3 crystal optically pumped by the output of the YLF laser and finally, it is compressed back to its initial 65-fs length. During this procedure the energy in pulse increases to 1 mJ. With the repetition rate of 1 kHz the average output power is around 1 W.

After the Odin amplifier the beam is divided into two separate branches by a beam-splitter. 70% of the beam power is used for the optical excitation of a sample. The arrival of the pump pulse is controlled with the delay line DL_1. Crystals for a second-harmonic- or third-harmonic generation (LBO and/or BBO crystals) can be placed in this branch, providing 400 or 266 nm excitation. In some experiments a beam expander consisting of a convergent and a divergent lens is used to ensure a homogenous excitation of large samples.

The remaining 30% passes through two diaphragms placed in 65 cm distance, which are used for a precise adjustment of the beam position. After the second diaphragm a second beamsplitter is placed. It divides the beam in a 96/4 ratio, with the more intense part being used for the generation of THz radiation and the further attenuated weaker part for the detection of THz pulses by the electrooptic sampling method described in Section 1.3.2. Both these branches (THz probe and sampling) are also equipped with delay lines (DL_2 and DL_3) for a precise adjustment of the arrival time of the THz and the sampling pulse.

The THz branch starts (in a vacuum box to avoid water vapor absorption of THz radiation) with the THz emitter which is a 1-mm-thick [011] ZnTe crystal. The THz beam is focused by an ellipsoidal mirror to the sample and by a second one onto another 1-mm-thick [011] ZnTe crystal which serves for the gated detection of THz radiation.

During the work on this thesis we used experimental geometries for OPTP experiments shown in Fig. 2.2. During the progress of the work on this thesis the experimental setup was upgraded from the one shown shown in Fig. 2.2a through Fig. 2.2b to Fig. 2.2c. The scheme shown in Fig. 2.2a is a non-collinear setup which is used for the measurements of slow dynamics (tens and hundreds of picoseconds). Here the oblique incidence of the excitation beam limits the time resolution to ≈1.5 ps.

A better time resolution is achieved if the second or the third (collinear) experimental setups are used (Fig. 2.2b and Fig. 2.2c). In these collinear setups, the whole probed area is excited at the same time. The key element in the scheme related to Fig. 2.2b is an ITO-coated optical-glass (BK7) beamsplitter. ITO (indium tin oxide) is transparent for visible radiation and simultaneously highly conductive, so that it acts as an efficient reflector for THz pulses. Moreover, an anti-reflective coating was deposited on the rear side of the beam-splitter to eliminate the losses of the excitation beam due to Fresnel reflections, namely multiple internal reflections which would cause an additional delayed excitation of the sample. In contrast, in the experimental setup shown in Fig. 2.2c an

element transparent for the THz and highly reflective for the pump beam is installed. This element is a fused-silica beamsplitter coated on the front side with reflective coating for the pump wavelength. The 45° angle of the incidence of the THz beam is close to the Brewster angle for the p-polarization.

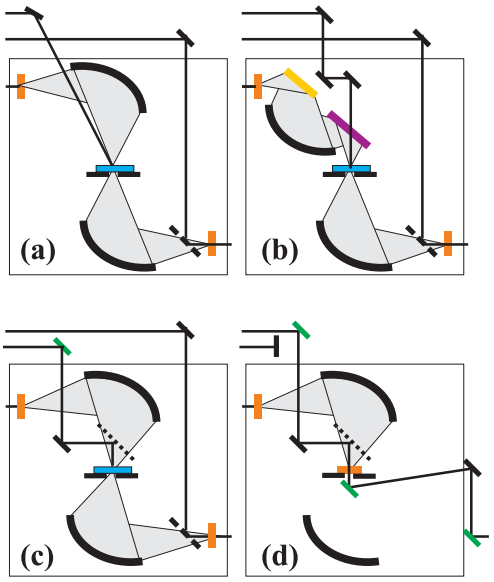

Figure 2.2: Schemes of the used setups for time-resolved measurements: (a) non-collinear setup for slow dynamics; (b) collinear experimental setup with ITO and antireflective coating BK7 beam-splitter (violet) and metallic THz mirror (yellow); (c) a collinear setup with a fused-silica beam-splitter transparent for THz radiation with a reflective coating for the pump-beam wavelength (dotted line); (d) an experimental setup for the measurement of the THz field at the sample position derived from the scheme (c). Green mirrors are mounted on a flipper holders.

In front of the ZnTe detector a pellicle beam splitter is placed. It is transparent for the THz beam and simultaneously it reflects the sampling beam in order to achieve a collinear propagation of both beams through ZnTe sensor. The polarization of the sampling pulse is changed from linear to circular in a Soleil-Babinet compensator (used as an adjustable $\lambda/4$ plate, Fig 2.1). Using a Wollaston prism the horizontal and vertical polarizations are spatially separated and detected by two balanced antiparallel photodiodes D_1 and D_2. The difference signal D_1-D_2, which is linearly proportional to the THz field in ZnTe, is transferred to a gated integrator and then to a lock-in amplifier. This signal is further normalized by voltage measured by the reference diode D_0.

An active beam-pointing stabilization of the laser system is ensured by a quadrant-photodiode detector (Fig 2.1). The horizontal and vertical offsets of the beam position

are canceled by tilting the mirror (equipped by motorized knobs) placed just behind the femtosecond laser source.

Our experimental setup allows us to adjust precisely the arrival of all pulses: delay line DL_1 in pump branch controls the arrival of the excitation pulse in time t_e and delay lines DL_2 and DL_3 placed in the THz and sampling branch serve for the adjustment of the arrival time of THz probe pulse in time t_p and sampling pulse in time t which maps the shape of the freely propagating THz waveform. As only two time parameters are independent, it is convenient to define relative delays. If in the experiment the delay line DL_2, which determines the time t_p is during experiment held at the fixed position, the independent time domain variables are $\tau = t - t_p$ and $\tau_p = t_p - t_e$. The time τ (DL_3) is connected to the sampling of the THz pulse transmitted through the sample and; τ_p (DL_1) has the meaning of the pump-probe delay and characterizes the decay of the sample excitation.

In order to obtain the equilibrium properties of a sample two measurements are required. The first measurement is a reference measurement, where an empty sample holder is placed at the sample position and the detected reference waveform $E^D_{\mathrm{ref}}(\tau)$ is measured. In the second measurement the waveform, which passed through the sample in equilibrium, is obtained $E^D_{\mathrm{sam}}(\tau)$. As for the synchronous detection, we use a lock-in amplifier synchronized to a mechanical chopper (166 Hz). In both these measurements the chopper is placed in the THz probe branch and the pump beam is blocked.

The first insight into the dynamics of the photo-excited sample is usually made in a pump-probe (PP) scan. The PP-scan is a measurement where the value of the maximum of the transient waveform $\Delta E_{\max}(\tau_p) \equiv \Delta E(\tau_0; \tau_p)$ (i.e., for a fixed $\tau_{=}\tau_0$) is detected as a function of the pump-probe delay τ_p. The transient waveform is measured with the chopper placed in the pump branch. This scan represents the time evolution of the mean THz response of the photo-excited sample thus it reveals the time scales on which the dynamical properties of the sample change.

To obtain the properties of the photoexcited sample in the time τ_p after the photoexcitation several measurements are necessary. In this case the measurement of the non-excited sample $E^D_{\mathrm{sam}}(\tau)$ (sample in equilibrium) with the pump beam blocked and a chopper placed in the probe branch serves as the reference measurement. The waveform of the photoexcited sample at the time τ_p after photoexcitation $\Delta E^D(\tau, \tau_p)$ is obtained with the pump beam on and the chopper in the pump branch. If the dynamics of the sample is slow (typically tens or hundreds of picoseconds) typically 5-7 measurements at different pump-probe delays are performed. However, in the case of ultrafast dynamics the response of the photoexcited sample $\Delta E^D(\tau, \tau_p)$ is measured as a dense grid of data in (τ, τ_p) space (typically 10 × 10 ps with the step of 70 fs).

As it will be explained in the following paragraphs, it is in principle possible to reach a better time resolution than the probe pulse length in time-resolved THz spectroscopy (i.e. sub-ps resolution). To achieve that, it is necessary to carry out some additional measurements which allow for a proper deconvolution of instrumental functions. The most

important one is the determination of the THz waveform E_0^D incident on the sample. An erroneous measurement of this quantity can lead to artifacts in the data making impossible their correct interpretation. Fig. 2.2d shows an optimized scheme we developed for this purpose. It is possible to convert the pump-probe scheme Fig. 2.2c to Fig. 2.2d within 10 minutes and to measure E_0^D before and after the time-consuming time resolved measurement. The immediate double measurement of this reference quantity allows us to check the stability of the setup during the time extended measurements. To pass from Fig. 2.2c to Fig. 2.2d it is only necessary to place the sensor into the sample holder (measurement of the waveform at the sample position) and to flip the flipping mirrors (in green in Fig. 2.2c and Fig. 2.2d) into the sampling path.

2.3 Methods of the time-domain THz spectroscopy

THz time-domain spectroscopy has been successfully applied to both the characterization of materials in the steady state (equilibrium spectroscopy) and in a photo-excited state (non-equilibrium spectroscopy). The main goal for equilibrium systems is to determine the complex dielectric response represented by complex refractive index N, complex conductivity σ or complex permittivity ϵ at THz frequencies. These quantities are connected via relations:

$$\sigma(f) = -2\pi \mathrm{i} f \epsilon_0 \epsilon(f) \qquad \text{and} \qquad \epsilon = \sqrt{N(f)} \tag{2.1}$$

Usually, these properties are determined by means of transmission measurements. Reflectance measurements can be useful when the sample is not sufficiently transparent at THz frequencies.

In non-equilibrium (i.e. photoexcited) systems the temporal evolution of the transient conductivity or permittivity can be directly extracted from either THz emission of optically photoexcited samples or optical-pump THz-probe experiments. Upon photoexcitation, free carriers are created and under suitable conditions they can start to emit THz photons or they may interact with the probing THz pulse; in both cases the measured THz signal reflects the dynamics of the carriers. This signal can be interpreted using various models (mentioned later), which provide valuable insight into the physical processes in the studied material. Experimental schemes of these methods are shown in Fig. 2.3.

2.3.1 Steady-state spectroscopy

2.3.1.a Transmission spectroscopy

The time-domain THz transmission spectroscopy (TDTTS) has become now a standard method for characterization of the dielectric properties of single crystals, thin films or

composite materials which are sufficiently transparent in the THz range. See e.g. [66], [67] for a review.

The dielectric properties of a sample are fully determined from two consecutive measurements. In the first one, a waveform of the THz pulse transmitted through the sample $E^{\mathrm{sam}}(\tau)$ is measured while in the second measurement the waveform transmitted through a reference sample $E^{\mathrm{ref}}(\tau)$ is acquired (usually an empty sample holder). From these data the transmission function defined as

$$T(f) = \frac{T^{\mathrm{sam}}(f)}{T^{\mathrm{ref}}(f)} = \frac{E^{\mathrm{sam}}(f)}{E^{\mathrm{ref}}(f)} \tag{2.2}$$

can be evaluated; here $E^{\mathrm{sam}} = T^{\mathrm{sam}}E_0$; $E^{\mathrm{ref}} = T^{\mathrm{ref}}E_0$ and the E_0 is the THz waveform incident on the sample.

The measured time-domain waveforms $E^D_{\mathrm{sam}}(t)$ [and $E^D_{\mathrm{ref}}(t)$] can be described as a convolution of the THz waveform incident on the sample $E_0(t)$ with all the instrumental functions, which influence the THz propagation and the detection process [including the reflection on the mirrors and the beam focussing, $P(t)$, and the sensor spectral response $D(t)$]. In frequency domain we obtain:

$$E^{\mathrm{sam}}(f) = E_0(f) \cdot T^{\mathrm{sam}}(f) \cdot P(f) \cdot D(f) \tag{2.3}$$

The various experimental functions on the right-hand side of this equation are difficult to obtain. A careful reference measurement allows one to eliminate these unknown

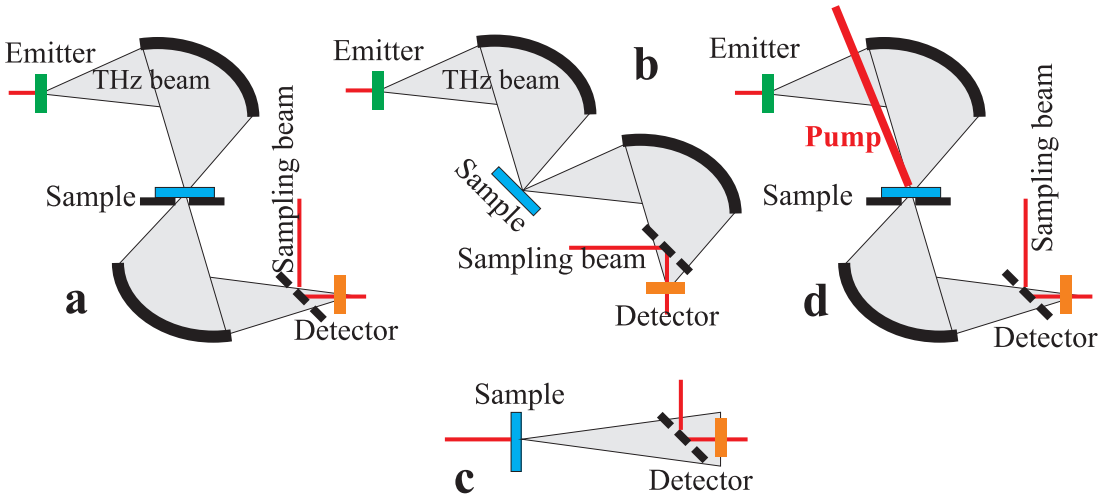

Figure 2.3: Basic TDTS experimental setups: (a) transmission, (b) reflection, (d) optical pump-THz probe and (c) emission. Four parabolic mirrors are often used instead of a pair of elliptical mirrors.

apparatus functions:

$$T(f) = \frac{E^{\mathrm{sam}}(f)}{E^{\mathrm{ref}}(f)} = \frac{E_0(f)\,T^{\mathrm{sam}}(f)P(f)D(f)}{E_0(f)\,T^{\mathrm{ref}}(f)P(f)D(f)} = \frac{T^{\mathrm{sam}}(f)}{T^{\mathrm{ref}}(f)}. \tag{2.4}$$

As it will be shown later, such straightforward simplification is not possible in pump-probe experiments, therefore we stress the principle of the elimination of instrumental functions at this place.

Assuming the conditions: (a) the sample is a plane-parallel plate, (b) the sample is placed in the air, (c) the THz beam is collimated and (d) the THz beam irradiates the sample at normal incidence, the propagation through the sample T^{sam} can be simply evaluated as a function of the complex refractive index $N(f) = n(f)+\mathrm{i}\kappa(f)$ and its thickness d [68]:

$$T^{\mathrm{sam}}(f) = \frac{4N}{(N+1)^2}\exp\left(\frac{2\pi\mathrm{i}fNd)}{c}\right)\sum_{j=0}^{\infty}\left(\frac{N-1}{N+1}\right)^{2j}\exp\left(\frac{4j\pi\mathrm{i}fNd}{c}\right) \tag{2.5}$$

The first term at the right-hand-side stands for Fresnel losses due to the direct transmission through the boundaries, the second (exponential) term stands for the direct propagation through the sample and the sum (last term) describes the contribution of internal reflections in the sample. The expression for the reference transmission (sample removed from the beam path) is much simpler:

$$T^{\mathrm{ref}}(f) = \exp(2\pi\mathrm{i}fd/c) \tag{2.6}$$

Finally, the transmission T is related to complex refractive index N through:

$$T(f) = \frac{4N}{(N+1)^2}\exp\left(\frac{2\pi\mathrm{i}fd(N-1)}{c}\right)\sum_{j=0}^{m}\left(\frac{N-1}{N+1}\right)^{2j}\exp\left(\frac{4j\pi\mathrm{i}fNd}{c}\right), \tag{2.7}$$

where m is the number of reflections (echoes) inside the sample which are taken into account. These reflections are experimentally resolved (at least for thick samples) and form separate pulses in the measured signal so that the value of the coefficient m can be easily determined (see Fig. 2.4a,b). In the case of an optically thin sample, where the internal reflections overlap, the geometrical series should be summed up to infinity.

Equation 2.7 constitutes two real equations for two real parameters n and κ; e.g., for $j = 0$ the expressions for the modulus t and the phase φ of the transmission function take the form [69]:

$$|t| = \frac{2\sqrt{n^2+\kappa^2}}{(n+1)^2+\kappa^2}\exp\left(\frac{-2\pi fd\kappa}{c}\right) \qquad \text{and} \tag{2.8}$$

$$\varphi + 2\pi l = \frac{2\pi f(n-1)d}{c} - \arctan\left(\kappa\frac{n^2+\kappa^2-1}{n(n+1)^2+\kappa^2(n+2)}\right) \tag{2.9}$$

The first right-hand side term of Eq. 2.9 accounts for the decrease of the phase velocity during the propagation in the sample, while the second one describes the phase change at the interfaces. The phase ranges from 0 to 2π; the integer l allows one to obtain the correct order of the phase displacement, which corresponds to the time delay of the THz probe pulse due to its propagation through sample. It can be estimated for the central frequency f_c of the THz pulse $l \approx \Delta t f_c - \varphi/2\pi$, where Δt is the measured time delay between the signal and the reference pulses: $\Delta t \approx (n-1)d/c$. The equations can then be solved numerically for n and κ. The same approach is in principle valid if $j \neq 0$: one obtains slightly more complicated expressions analogous to Eq.2.8 and Eq.2.9 which can be solved numerically.

In the case of a thin film sample on a transparent substrate the situation is similar to the case of a bulk sample, but in a reference measurement a substrate without the thin film sample is measured. Mathematically a thin film on a substrate has to be treated as a two-layer system. In this case the expression of the complex transmission function is more complicated [70], [71] (in this formula $j = 0$ in a sense of multiple reflections on the substrate):

$$T(f) = \frac{2N_f(N_s+1)\exp\left[2\pi \mathrm{i} f(N_f-1)d_f/c\right]\exp\left[2\pi \mathrm{i} f(N_s-1)(d_s-d_s')/c\right]}{(1+N_f)(N_f+N_s)+(1-N_f)(N_f-N_s)\exp\left[4\pi \mathrm{i} f N_f d_f/c\right]} \tag{2.10}$$

where N_f and N_s are complex indices of the film and substrate; d_f is the thickness of the film, d_s and d_s' are thicknesses of the substrate with and without the thin film, respectively (Fig. 2.4c).

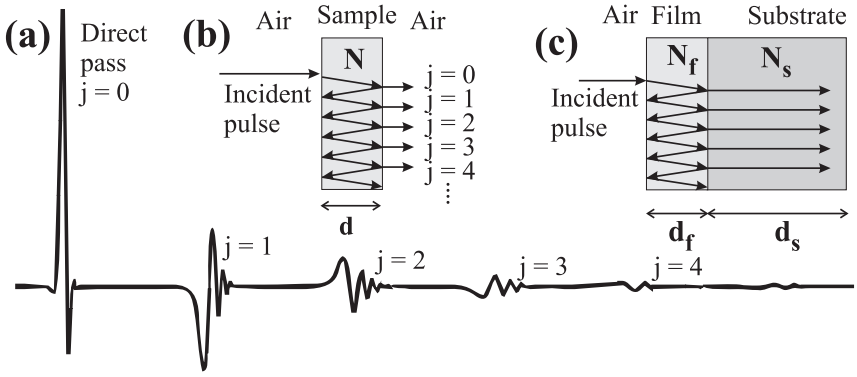

Figure 2.4: (a) Reflections in thick samples. The numbering of echoes coincides with the j value indexing the terms in the sum in Eq. 2.7. (b) Scheme of internal reflections in a dispersive thick sample. The spatial separation of echoes is used only for their graphical resolution; practically, it vanishes. (c) Scheme of internal reflection in sample on a substrate.

2.3.1.b Reflection spectroscopy

The time-domain THz reflection spectroscopy (TDTRS) is used instead of TDTTS in two special cases. Firstly, when the sample is not transparent in the THz range and secondly, if a thin film sample does not offer a sufficient sensitivity to provide precise information about the optical constants in the transmission setup. In the latter case, the determination of the THz properties of the thin film on a substrate in transmission is sometimes inaccurate due to the fact that the small phase change induced by the thin film may be comparable to the phase uncertainty related to the THz propagation through (thick) substrate. On the other hand, in TDTRS the reflections on the air/thin-film/substrate interfaces are not affected by the uncertainty in the substrate thickness.

In order to determine the reflectivity R of an unknown sample a reference measurement of a sample with known characteristics is required.

$$R(f) = \frac{E^{\mathrm{sam}}(f)}{E^{\mathrm{ref}}(f)} \tag{2.11}$$

The reference sample is usually a metallic mirror. Assuming that an ideal mirror is used as a reference and the reflection from the front surface of the sample can be temporally separated from the reflection coming from its rear surface, the reflectivity can be expressed as [72]:

$$R = \frac{N^2\cos\theta - \sqrt{N^2 - \sin^2\theta}}{N^2\cos\theta + \sqrt{N^2 - \sin^2\theta}} \quad \text{TM polarization} \tag{2.12}$$

$$R = \frac{\cos\theta - \sqrt{N^2 - \sin^2\theta}}{\cos\theta + \sqrt{N^2 - \sin^2\theta}} \quad \text{TE polarization} \tag{2.13}$$

where θ is the angle of incidence of the THz beam.

2.3.2 Time-resolved spectroscopy

Terahertz time-resolved spectroscopy is used to study solid-state materials, liquids and gases after the excitation of ultrashort laser pulses. It can achieve sub-ps resolution and using this method typically processes lasting up to nanosecond are studied. As THz radiation interacts with mobile carriers, or accelerated mobile carriers can generate the THz radiation, these methods are widely used to study photoinduced conductivity of free and weakly localized carriers, their lifetimes and mobilities. Furthermore, in semiconductors effect from intervalley electron scattering [73] to Coulomb screening in a photoexcited electron-hole plasma [74] are being studied.

2.3.2.a Emission spectroscopy

THz emission spectroscopy (TES) is a spectroscopic method investigating processes in which the THz emission occurs. In TES THz pulses emitted from photoexcited samples are used to analyze photoinitiated carrier dynamics or polarization. Detected THz field far from the emitter is proportional to the time-derivative of the transient current flowing through the emitter, which makes it possible to investigate the carrier density evolution and/or the time-dependent carrier velocity. As the temporal resolution of TES is defined rather by the length of the optical excitation pulses and the detector response than by the THz pulse length, ultrashort femtosecond pulses are used to excite the emitters, leading to sub-picosecond temporal resolution. TES is mostly used to study the dynamics in semiconductors or semiconductor heterostructures [75], [76]. When *p-i-n* diodes are exposed to ultrashort laser pulses shorter then 20 fs, different transport regimes ranging from initial ballistic transport over velocity overshoot to steady state drift current can be studied [77–80].

2.3.2.b Optical-pump THz-probe spectroscopy

In optical-pump THz-probe (OPTP) experiments samples under investigation are first excited by an ultrashort femtosecond pulse and subsequently probed by a delayed THz pulse.

The photo-induced response of the sample can be extracted from the time-dependent transient conductivity $\Delta\sigma$ or permittivity $\Delta\epsilon$. Because the energy of the THz photons is low, OPTP spectroscopy constitutes an excellent non-destructive contactless electrical probe of various transport processes.

Undopped semiconductors belong to a group of materials which are extensively studied using the OPTP method. In their steady-state they are transparent to THz radiation, however, after photoexcitation free carriers are created, which strongly interact with THz radiation. This makes the OPTP spectroscopy an ideal tool for investigating the evolution of the free-carrier concentration along with a time-dependent mobility in semiconductors. Besides the studies of carrier dynamics in semiconductors, this method was successfully applied to study superconductors [81], gasses [82] and liquids [83]. A review of studies on different types of materials can be found in [84] or [67].

The experimental setup is very similar to the transmission experiment, only an excitation (pump) beam is added (see for example Fig. 2.5). The wavelength of the pump beam can be changed by nonlinear conversion. All three branches (THz, sampling and excitation branch) are equipped with delay lines which allow for a perfect synchronization of the arrival times of pump, probe and sampling pulses. However, to control the arrival time of all mentioned pulses it is necessary to control only two of these delay lines while the third delay line may stay at the fixed position. In our experiments we do not move with line DL_2, which controls the arrival of the THz pulse (it is held at the fixed position).

Remaining two delay lines control (1) the time τ which is connected to the sampling of the THz pulse transmitted through the sample and it has the meaning of the real time with respect to the THz pulse; (2) τ_p which is the pump-probe delay and characterizes the decay of the sample excitation (these two time variables are in the Fourier space represented by angular frequencies ω and ω_p).

The wave equation, which describes the propagation of electromagnetic field (in our case THz probing field) in a photoexcited medium, can be solved analytically in the Fourier space within the approximation of the small photoinduced signal (photoinduced signal ΔE is small compared to the incident THz field E_0) $\Delta E \ll E_0$. One finds for the outgoing transient part of the THz field [85], [86]:

$$\Delta E(\omega, \omega_p) = \frac{\Delta\sigma(\omega, \omega_p)}{\mathrm{i}\omega\epsilon_0}\Xi(\omega, \omega - \omega_p)E_0(\omega - \omega_p) \tag{2.14}$$

Ξ is a transfer function which can be in a general case complicated [87]. It depends on the ground state properties of the sample and on the experimental geometry. However, for thin film samples it is $\propto \mathrm{i}\omega$.

Generally, different parts of the THz waveform experience a different delay with respect to the excitation event, resulting in a frequency mixing which appears in the argument of the incident THz waveform $E_0(\omega - \omega_p)$ in Eq. 2.14. This term dramatically complicates evaluation of the photoinduced conductivity $\Delta\sigma$.

When the studied dynamics is slow, i.e. when it occurs on a time scale much longer than the length of the probing THz pulse (2 ps), the frequency mixing can be neglected, i.e. relevant ω_p for which $\Delta\sigma(\omega, \omega_p)$ reaches non-zero values is below the THz range: $\omega_p \ll \omega$. This implies that the Fourier transformation $\tau_p \rightarrow \omega_p$ is not necessary for the data analysis.

In this case the transient conductivity $\Delta\sigma$, can be directly evaluated from the ratio of the detected transient signal and the detected reference signal $\Delta E^D / E^D_{\mathrm{ref}}$, as the instrumental functions terms and terms of the incident THz field E_0 cancel out [c.f. Eqs. 2.2-2.4]. One finally finds:

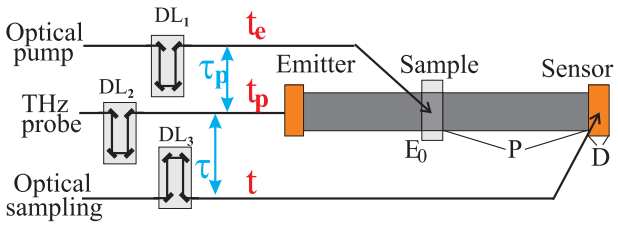

Figure 2.5: Scheme of OPTP technique. For definition of symbols, see text.

$$\Delta\sigma(\omega,\tau_p) = \frac{\mathrm{i}\omega\epsilon_0 T^{\mathrm{sam}}(\omega)\Delta E^D(\omega,\tau_p)}{\Xi(\omega,0)E^D_{ref}(\omega)} \tag{2.15}$$

On the other hand, if the investigated dynamic is comparable to or faster than the THz pulse length, much more elaborate calculation including a 2D Fourier transformation needs to be performed.

In both cases, ΔE is not measured directly because it represents the transient field just leaving the sample (near field). The detected transient signal ΔE^D can be obtained as a convolution of ΔE and the instrumental functions P and D describing the propagation of the THz pulse between the sample and the sensor and the response of the sensor itself, respectively. In the frequency domain the relation reads:

$$\Delta E^D(\omega,\omega_p) = D(\omega)P(\omega)\Delta E(\omega,\omega_p) \tag{2.16}$$

The presence of the instrumental functions in the formula for the detected signal implies that a reference measurement has to be carried out. A convenient reference measurement consists in acquiring the THz signal transmitted through optically unexcited sample (i.e. in its equilibrium state):

$$E^D_{\mathrm{ref}}(\omega) = D(\omega)P(\omega)E_0(\omega)T^{\mathrm{sam}}(\omega) \tag{2.17}$$

T is the complex equilibrium transmission function of the sample [c.f. Eq. 2.3].

In the ratio $\Delta E^D/E^D_{\mathrm{ref}}$ the terms of the THz incident field $E_0(\omega)$ and $E_0(\omega-\omega_p)$ do not cancel each other:

$$\frac{\Delta E^D(\omega,\omega_p)}{E^D_{\mathrm{ref}}(\omega)} = \frac{\Delta\sigma(\omega,\omega_p)\Xi(\omega,\omega-\omega_p)T^{\mathrm{sam}}(\omega)}{\mathrm{i}\omega\epsilon_0}\frac{E_0(\omega-\omega_p)}{E_0(\omega)} \tag{2.18}$$

As a consequence, the incident THz field E_0 has to be determined in a separate measurement. In order to achieve that the measurement should be carried out in the setup with the sensor placed at the position of the sample (see Fig. 2.2d). The result of such a measurement is a waveform E^D_0 related to E_0 through the expression:

$$E^D_0 = DE_0 \tag{2.19}$$

I.e., a term $D(\omega-\omega_p)$ will also appear in Eq. 2.18.

When the bandwidth $\Delta\omega_L$ of the sampling optical pulse is much smaller than its carrier frequency ω_L the response function of the detector $D(\Omega)$ as a function of a general frequency variable Ω can be written in a form:

$$D(\Omega) = \frac{2n}{n+1}\chi^{(2)}_{\mathrm{eff}}(\omega_L,\Omega,\omega_L-\Omega)\mathrm{e}^{\mathrm{i}\varphi}\frac{\sin(\varphi)}{\varphi}G(\omega) \tag{2.20}$$

The first term in this expression represents the Fresnel losses at the detector-air interface. The second term introduces Pockels coefficient dispersion for THz frequencies, which is treated as a constant value.

In the third term $\varphi = \Omega\Delta n(\Omega, \omega_L)/c$. The term accounts for the waveform distortion due to the dispersion of the sensor with length l and due to the velocity mismatch given by difference between the optical group refractive index n_g of the sampling pulse and the THz refractive index n: $\Delta n(\Omega, \omega_L) = n(\Omega) - n_g(\omega_L)$. Finally, the last term in Eq. 2.20 is the Fourier transformation of the intensity profile. It describes the broadening of the THz waveform owing to the finite temporal length of the optical sampling pulse.

The sensor response function is measured, when the sensor is treated as a sample in a equilibrium-like measurement. It means that the waveform of the THz signal transmitted through the sensor $D(\tau)$ and a reference waveform of the empty sample holder $E^D_{\mathrm{ref}}(\tau)$ needs to be detected. The response function, which characterizes the sensor, is for the given sensor measured only once. The sensor's instrumental function can be derived from the ZnTe THz spectrum Fig. 2.6. The optical group refractive index n_g can be evaluated from a measurement, where the ZnTe sensor is placed in the sampling branch. Its presents shifts in time the arrival of the sampling pulse and from the knowledge of time delay the thickness of the sensor n_g is determined.

Finally, the expression for the complex conductivity reads:

$$\Delta\sigma(\omega, \omega_p) = \frac{\mathrm{i}\omega\epsilon_0 T^{\mathrm{sam}}(\omega)\Delta E^D(\omega, \omega_p)E^D_0(\omega)D(\omega - \omega_p)}{\Xi(\omega, \omega - \omega_p)E^D_{ref}(\omega)E^D_0(\omega - \omega_p)D(\omega)} \tag{2.21}$$

This method allows us to obtain directly the photoinduced conductivity without any assumption about its behavior. Photoconductivity $\Delta\sigma(\omega, \omega_p)$ can be experimentally obtained only in the spectral range, where both ΔE^D and E^D_{ref} exceed the noise level. Fig.

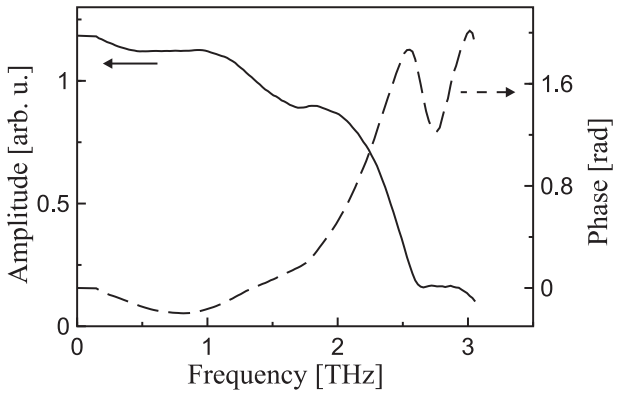

Figure 2.6: Instrumental function $D(f)$ of our ZnTe sensor.

2.7 shows the accessible region in the 2D (ω, ω_p) space. Several border lines, which are related to different terms in Eq. 2.21, limit the accessible frequencies [86]. The origin of the diagonal spectral delimiters can be found in the terms with the argument $(\omega - \omega_p)$ where the frequency mixing occurs. For example the accessible area is strongly reduced due to the diagonal character of the upper limit of the spectral sensitivity of the sensor. For a typical THz experiment based on a ZnTe emitter and sensor, one obtains $|\omega|, |\omega - \omega_p| < 2,5$ THz. For more details, see [86].

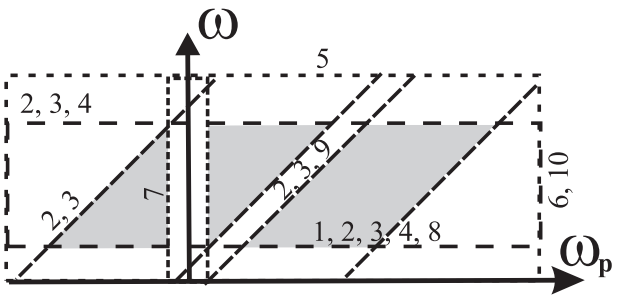

Figure 2.7: Experimentally accessible areas of $\Delta\sigma$ (gray) in frequency space (ω, ω_p). Border lines are related to: (1) temporal windowing; (2) spectrum of incident pulse; (3) sensor; (4) sample in equilibrium state; (5) sampling rate τ; (6),(7) scan length in τ_p; (8) transfer function Ξ; (9) diffraction and (10) pump pulse length. After [86].

2.3.3 Models of slow dynamics conductivity

By "slow" dynamics we mean processes which are slower than the pulsewidth of the probing THz pulse. The lack of frequency-mixing terms in Eq. 2.15 makes the mathematical description of the slow dynamics much simpler. In this quasi-static approximation the dynamic response can be written in the factorized form:

$$\Delta\sigma(\omega, \tau_p) = \sum_i n_i(\tau_p) f_i(\omega), \tag{2.22}$$

where the sum is made over contribution to the THz response of all possible dynamical processes. Each process is characterized by its spectral response function $f_i(\omega)$ and the decay of the density of elementary excitations $n_i(\tau_p)$ (i.e. carrier density in semiconductors). Possible conductivity models, which may correspond to individual terms in the sum are as follows.

2.3.4 Drude model

The simplest description of free carriers in response to an applied electric field in a doped or photoexcited semiconductors (or other conducting material) is given by the Drude model. Typically, this model is used to describe free carriers in semiconductors with ultrafast response such as low-temperature-grown GaAs [88], [89], [90] radiation-damaged silicon on sapphire [91], [3], InGaAs [73] etc. Moreover, it can be also used to explain the dynamics of carriers after multiphoton ionization in fluids [92]. Drude model describes free carriers whose wave functions are delocalized (i.e. the restoring force is absent). The Drude spectral response is:

$$f_D(\omega) = \mu_D e \frac{1}{1 - \mathrm{i}\omega\tau_D}, \tag{2.23}$$

where τ_D is the momentum scattering time of the carriers; $\mu_D = \frac{e}{m^*}\tau_D$ is their microscopic mobility and m^* is their effective mass. In this model the DC-conductivity ($\Delta\sigma_{DC} = ne\mu_D$) is non-zero ($\sigma_{DC} \neq 0$) and the real part of the permittivity is negative (Re $\epsilon < 0$) what means that the system has a capacitive response.

2.3.5 Relaxator model

Debye relaxator which is a simplified overdamped oscillator [93], describes the response of localized carriers (localization in a well or caused by hopping of carriers). The spectral response of this model reads:

$$f_R(\omega) = -\mu_R e \frac{\mathrm{i}\omega\tau_R}{1 - \mathrm{i}\omega\tau_R}, \tag{2.24}$$

where $1/\tau_R$ is relaxation frequency, and μ_R represents carriers mobility [94]. In contrast to the Drude model, the carriers feel the restoring force so they do not contribute to DC conductivity. Moreover, the real part of the permittivity is positive, which refers to capacitive response of the system. The conductivity increases with frequency and in the high-frequency regime ($\omega\tau_R > 1$) it saturates: $\Delta\sigma_{\mathrm{R},\infty} = ne\mu_R$.

2.3.6 Hopping model

Hopping model proposed by Dyre [95] describes hopping of carriers between spatially randomly distributed energetic barriers (with varying energy of the barrier). It has features similar to the Debye relaxator ($\Delta\sigma_{\mathrm{H},\infty} = ne\mu_H$), however, it was shown that this model can be applied over several frequency decades [95]:

$$f_H(\omega) = \mu_H e \mathrm{i}\omega \left[1 - \frac{\ln(\tau_{\min}) - \ln(\tau_{\max})}{\ln(1 - \mathrm{i}\omega\tau_{\min}) - \ln(1 - \mathrm{i}\omega\tau_{\max})}\right] \ln(\tau_{\max}/\tau_{\min})/(1/\tau_{\min} - 1/\tau_{\max}), \tag{2.25}$$

where $1/\tau_{\max}$ and $1/\tau_{\min}$ are low and high cutoff frequencies, respectively, which roughly delimit the range of the conductivity dispersion.

2.4 Models of fast dynamics conductivity

2.4.1 Drude model

The models describing the carrier dynamics have to be formulated in the two dimensional frequency domain. The photoinduced complex Drude conductivity of the delocalized carriers is [85]:

$$\Delta\sigma(\omega,\omega_p) = \frac{e\mu'_D n_{D,0}}{1+\tau'_D/\theta'_D - \mathrm{i}\omega/\tau'_D}\frac{1}{1/\theta'_D - \mathrm{i}\omega_p} \tag{2.26}$$

θ'_D is the lifetime of the carriers, $n_{D,0}$ is their initial concentration and τ'_D is their momentum scattering time. The mobility in this model is $\mu'_D = \frac{e}{m^*}\tau'_D$. The conductivity shows a single pole in $\omega = \omega_p = 0$. The amplitude of the conductivity decreases with increasing frequencies; the speed of this decrease along ω and ω_p is a measure of τ'_D (compare Fig. 2.8a,c,d) and θ'_D (compare Fig. 2.8a,b), respectively.

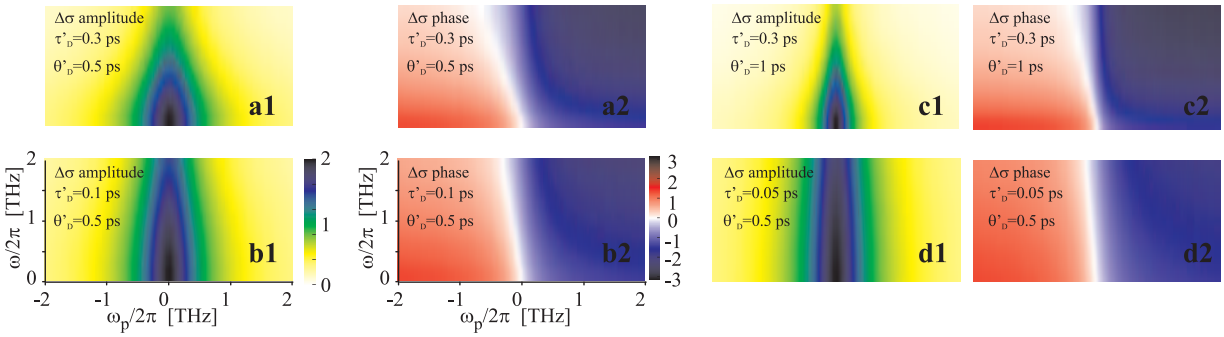

Figure 2.8: Modeling of ultrafast photoexcited conductivity (color) by Drude model $\Delta\sigma(\omega/2\pi, \omega_p/2\pi)$. Graphs 1 represent amplitude, graphs 2 represent phase. a: scattering time $\tau'_D = 0.3$ ps, lifetime of carriers $\theta'_D = 0.5$ ps; b: $\tau'_D = 0.1$ ps, $\theta'_D = 0.5$ ps; c: $\tau'_D = 0.3$ ps, $\theta'_D = 1.0$ ps; d: $\tau'_D = 0.05$ ps, $\theta'_D = 0.5$ ps

2.4.2 Overdamped relaxator model

The response of the Debye relaxator in the two dimensional frequency domain reads:

$$\Delta\sigma(\omega,\omega_p) = \frac{e\mu'_R n_{R,0}}{1-\mathrm{i}\omega/\tau'_R}\frac{-\mathrm{i}\omega + 1/\theta'_R}{-\mathrm{i}\omega_p + 1/\theta'_R} \tag{2.27}$$

where θ'_R is the lifetime of the carriers and $n_{R,0}$ is their initial concentration. As in the preceding model, the extent of the conductivity in the ω_p direction is determined by the

carrier density lifetime θ'_R (compare Fig. 2.9a,b). In contrast to the Drude model, the amplitude of the conductivity is here an increasing function of the frequency. The behavior of the model on the relaxation time τ'_R is shown in Fig. 2.9a,c,d. Note that the Relaxator model with high value of τ'_R (Fig. 2.9d) gives very similar results compared to the Drude model with parameter τ'_D small (Fig. 2.8d), where in both models is in this limit only weak dependance on ω.

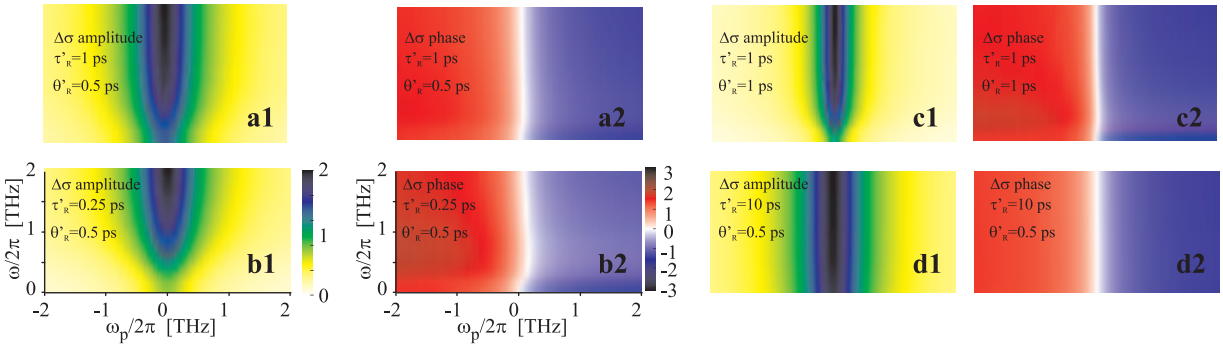

Figure 2.9: Modeling of ultrafast photoexcited conductivity (color) by Relaxator model $\Delta\sigma(\omega/2\pi, \omega_p/2\pi)$. Graphs 1 represent amplitude, graphs 2 represent phase. a: relaxation time $\tau'_R = 1.0$ ps, lifetime of carriers $\theta'_R = 0.5$ ps; b: $\tau'_R = 0.25$ ps, $\theta'_R = 0.5$ ps; c: $\tau'_R = 1$ ps, $\theta'_R = 1.0$ ps; d: $\tau'_R = 10$ ps, $\theta'_R = 0.5$ ps

Chapter 3

THz spectroscopy of semiconductors

When an intrinsic semiconductor is photoexcited with energy exceeding its bandgap energy, several stages of relaxation can be observed. Immediately after the photoexcitation by an ultrashort pulse the semiconductor is in a coherent regime, in which the carriers are in a well-defined phase relationship with the electromagnetic field that created them. In this regime phenomena which manifest the basis of quantum mechanics, such as Rabbi oscillations, photon echo or others can be studied. The coherence is destroyed after a short time by momentum- and energy-scattering mechanisms. The momentum relaxation occurs on a timescale from units to hundreds of femtoseconds via inelastic and elastic scattering. During this period carrier-carrier scattering of electrons (holes) drives the system from the non-thermal regime to the hot-excitation regime, which constitutes the so-called Coulomb thermalization. When it ends, the system can be described by a Fermi-Dirac distribution with a temperature which can be much higher than the thermal energy of the lattice and can be different for different types of carriers (electrons, holes...). Typically, this process occurs on a timescale of hundreds of femtoseconds. In contrast, the electrons and holes need approximately a couple of picoseconds to achieve a common temperature and finally, electron-hole pairs reach the lattice temperature within a few hundreds of picoseconds. This phonon-related relaxation of energy is realized via various interactions with phonons. The holes interact primarily with optical phonons with small wave-vector; on the other hand, large wave-vector phonon emission or absorption leads to the scattering of electrons from the central valley (Γ) to the side valleys (intervalley scattering).

At the end of hot-carrier regime all electrons (holes) are at the bottom of conduction (valence) band and have the same temperature as the lattice. These initially free carriers can be trapped for a short time in shallow or for a long time in deep energetic traps and become immobile. For high carrier densities three-body non-radiative Auger recombination may occur after the first 100 ps. Other recombination processes take place on even longer time scales and therefore have only negligible contribution within the ultrashort time domain investigated in this work.

One of methods suitable for the study of the dynamics of carriers on the ultrashort

timescale is Time-Resolved THz spectroscopy (TRTS). This non-contact probe method can determine complex frequency-dependent far-infrared permittivity or conductivity. TRTS is used to study ultrafast changes in material's properties upon photoexcitation with an optical pump pulse, which marks the time origin with respect to the above described carrier relaxation properties.

A typical THz experimental setup allows for the study of photoexcited samples up to 1 ns after photoexcitation. In most commonly used experimental setups with ∼50 - 100-fs-long excitation pulses the time resolution is better than 200 fs [88]. Note however, that the TRTS experiments with multi-THz pulses (i.e. probe pulses centered at 28 THz) have been successfully carried out [96]; in this case nearly ten times better resolution was achieved with much shorter excitation pulses.

Many highly interesting phenomena can be studied on the sub-picosecond timescale. The semiconductors are transparent to THz radiation in their ground state. However, carriers created during the photoexcitation strongly interact with THz radiation. On the fastest timescale one can investigate many-particle interactions developed after excitation [96], intervalley scattering and/or carrier cooling (via the mobility changes in various conduction band states) [73] or ultrafast trapping of carriers [4]. On longer timescales the intersubband transitions in quantum heterostructures or decay and formation of excitons in GaAs multiple QWs [97] can be observed.

The magnitude of the change of the THz transmission due to photoexcitation is, in most cases, proportional both to the free carrier mobility and to their density. TRTS with its high sensitivity to mobile carriers can be used to detect carrier densities as low as $5 \times 10^{14}\mathrm{cm}^{-3}$ in GaAs with the skin depth of 1 micrometer [67]. In semiconductors the spectral response has mostly a Drude-like fingerprint. The THz region is very convenient for probing semiconductors because the frequency range closely matches typical carrier scattering rates of 10^{12} to $10^{14}\mathrm{s}^{-1}$, allowing for more accurate modeling of the photoconductivity data. In this spectral region also the plasma frequency of photoexcited carriers can be studied.

Besides the classical Drude model introduced in Section 2.3.4, the response of delocalized carriers in semiconductors can be characterized by models such as the Cole-Davidson model (doped semiconductors) [98] or Cole-Cole model [88]. On the other hand, in the case of carriers trapped in a shallow energetic trap, when the localization still allows them to interact with THz radiation, their conductivity can be described by a Debye relaxator (Sec. 2.3.5) or a hopping model (Sec. 2.3.6). Moreover, using a combination of TRTS and appropriate models quasiparticles such as excitons and polarons, which exhibit unique spectral signatures in the THz range, can be studied.

The access to both concentration and mobility of carriers simultaneously is an advantage when compared to methods such as optical transient absorption or time-resolved luminiscence, which are sensitive to either the sum or the product of electron and hole distribution functions, respectively. In addition, luminiscence methods are limited to direct-gap materials, whereas TRTS can be used to study carrier dynamics also in indirect-gap

materials like silicon. Even methods that are sensitive to the diffusion of carriers, such as four-wave mixing or transient grating, can determine in one measurement only conductivity at one frequency and are therefore not suitable for the determination of the frequency-dependent conductivity.

In this work various semiconductor systems were intensely studied using optical-pump THz-probe experiments with two goals in mind:

(A) to learn the properties and dynamics of semiconductors on the ultrafast timescale

(B) to take advantage of the ultrafast properties of semiconductors to demonstrate optically controlled modulation of THz radiation.

Within the part **(A)** we investigated two different semiconductor systems, namely ion-bombarded InP and microcrystalline silicon. The former is characterized by Drude transport of highly mobile carriers, which can be on the sub-picosecond timescale trapped in deep energetic traps or recombine due to defects caused by the heavy ion-bombardment [i]. This ultrafast material, whose properties like the ultrashort lifetime of carriers can be purposely adjusted, is of high interest for the field of applications in THz emitters, detectors or high-speed electronics and optoelectronic components. The latter system (microcrystalline silicon) is a disordered semiconductor, which is intensely studied due to its applications in cheap large-area solar cells. Our goal here was to characterize the transport of carriers on sub-picosecond to nanosecond timescale [ii], [iii].

Within the part **(B)** we first demonstrated the possibility of the modulation of THz radiation using a photoexcited GaAs wafer, where the modulation was controlled by a decrease in the intensity of the excitation beam [iv]. With this feasible modulator we achieved high contrast between on and off state in a broad band of frequencies. Then, our effort was focused on reaching substantially lower optical energies needed for the operation of the device while still preserving the high contrast. The solution was found in the enclosure of the GaAs wafer in the middle of a photonic crystal [v], [vi], making the modulator a resonant structure. Here we have studied both the material response and the response of the structure.

The results of our work were published in six papers in impacted scientific journals; these papers can be found in the Appendix of this thesis and are denoted by [i-vi] throughout the text.

3.1 Ultrafast carrier dynamics in InP

Indium Phosphide (InP) is a widely used direct-band semiconductor. The energy of the band gap (1.34 eV) allows for the excitation with 800 nm, which causes that free electrons are generated only in the Γ-valley (the energy needed for the excitation in the L-valley is 1.93 eV and for the X-valley is 2.19 eV). The penetration depth for the 800-nm excitation

is 300 nm (300 nm = $1/\alpha$). The mobility of carriers is well-known from the literature and reach values of 5000 $\mathrm{cm^2V^{-1}s^{-1}}$. The effective mass in Γ-valley is 0.08. [99].

The ultrafast dynamics in the InP sample was induced by the bombardment by heavy ions of Br^+ with the energy of 11 MeV [i]. The samples were prepared in collaboration with Institut d'Electronique Fondamentale in Orsay. Highly energetic heavy-ions damage the crystal lattice of InP; during their path in InP they create clusters of point defects (host atom displacement). The ions are subsequently stopped inside the sample in the depth of $\sim 3.5\mu$m. In this depth, the concentration of both types of defects, host atom displacement and implanted Br atoms, is the highest.

We studied how the implantation dose of Br^+ ions (doses of $10^9, 10^{10}, 10^{11}$ and $10^{12}\mathrm{cm^{-2}}$) influences the electron lifetimes and mobilities in two series of samples for which the preparation procedure differed. For the first series several different doses of Br ions were applied to bare InP wafers (samples B9 – B12). In these samples the concentration of Br atoms in the studied surface layer (given by the penetration depth of the excitation wavelength) was so small that it could not influence the dynamics. The ultrafast response was thus assumed to be ralated to the host atom displacement. The second type of samples was prepared in order to study the region of the highest defect concentration. Samples were first prepared with a protective 3μm thick InGaAs layer; after the bombardment, the layer was etched away (samples E9 – E11). The depth profiles of Br-atom implantation densities and densities of host atom displacement defects for both types of samples are shown in Fig. 1 [i]. For the same irradiation dose the density of host atom displacements in the B9 - B11 samples was smaller by a factor of 4.5 as compared to the E9 - E11 samples. In principle, the implanted Br atoms could play a role in the ultrafast trapping for samples E9 - E11. The defect densities for all samples are summarized in Table 1 [i].

The transient conductivity spectra of all samples exhibited a Drude response of free charge carriers. Except for the samples E11 and B12, where the dynamics was shorter than the length of the THz probe pulse, the conductivity spectra could be fitted by the Drude model in the quasistatic approximation (Eq. 2.23). An example of the transient conductivity spectra of the samples E9 and E10 fitted by the Drude model is shown in Fig.2a in [i]. The experimental transient conductivity and its fits of the samples E11 and B12 (see Fig. 3 in [i]) were analyzed within the frame of the method described in Sec. 2.4.1.

The mobility of the samples μ was evaluated from the momentum relaxation time τ_s using the relation $\mu = e_0\tau_s/m_{\mathrm{eff}}$, where m_{eff} is the effective mass of electrons and e_0 is an elementary charge. As τ_s was found to be independent of the pump-probe delay, the decrease of the signal in the pump-probe scans reflects only the population decay of free charge carriers. This is demonstrated in Fig 2b in [i] where we can compare the response times of the studied samples. The carrier population is well described by a single exponential decay with a time constant τ_{decay} and a constant contribution n_b, which arises mainly due to trap filling: $n(\tau_p) = n_0 \exp(-\tau_p/\tau_{\mathrm{decay}}) + n_b$, where n_0 is the initial carrier concentration and τ_p is pump-probe delay. Both parameters τ_{decay} and n_b depend on the

pump pulse intensity in the samples irradiated by smaller doses. These phenomena were attributed to the trap filling.

In order to better understand these effects we carried out measurements with variable excitation intensities for E9 and E10. The variation of the excitation intensity did not significantly influence the shape of spectral response of these samples, which implies that the momentum relaxation time remained unaltered. On the contrary, the pump-probe dynamics exhibited more complex features due to trap filling and diffusion of carriers. Since the carrier diffusion length ($l_{\mathrm{diff}} = \sqrt{D\tau_{\mathrm{decay}}}$, where D is the diffusion coefficient) in the samples E9 ($l_{\mathrm{diff}} \sim 690$ nm) and E10 ($l_{\mathrm{diff}} \sim 170$ nm) was found to be longer or comparable to the absorption length of the excitation beam, a part of photo-generated carriers diffuses away from regions with significantly filled traps into regions with nearly empty traps.

To model the behavior of carriers a simulation based on a set of partial differential equations, which included carrier trapping, trap filling and carrier diffusion, was developed (see appendix of paper [i]). Sets of 2 - 3 pump-probe scans measured at different excitation intensities were analyzed and the results fit the measured data well (see Fig. 4 in [i]). The model was able to distinguish the lifetimes contributions of electrons and holes (τ_e and τ_h, respectively); also, the density of traps N_t and their energy ΔE with respect to the bottom of the conduction band minimum could be estimated. For both samples the density of traps was found to be more than by an order of magnitude lower than the initial density of host atom displacements. This may be related to the fact that in the evaluation of the density of host atom displacements the annealing processes that occur a few picoseconds after the ion-irradiation were not taken into account. Nevertheless, even for the lowest excitation densities used in our experiments in the sample E9 the trap filing was observed, because of the low density of defects. The electron lifetime thus could not be determined precisely for this sample. This implies that lifetimes τ_{decay} of other samples with lower defect densities (B9, B10) have to be influenced as well and do not describe exactly the electron lifetime τ_c. For the samples with higher irradiation dose (B11, E11, B12) the trap density is higher than the initial carrier density, thus τ_{decay} is a reasonable approximation of τ_e.

In both series of samples the response time τ_{decay} was found to be inversely proportional to the nominal defect density. In the most irradiated sample, the carrier lifetime was reduced by three orders of magnitude (to 290 fs) in comparison to as-grown (non-bombarded) sample. The highest mobility was found in the least bombarded sample B9 with the lowest value of the defects concentration ($\mu = 3000$ cm^2/Vs). The same value of mobility was obtained in the as-grows InP reference sample. With the increase of the defect concentration the value of the mobility decreased. Nevertheless, for the most damaged sample B12 still a relatively high value of the mobility (900 cm^2/Vs) was obtained. The mobilities and lifetimes are shown in Fig. 5 in [i]. As can be clearly seen from the Fig. 5 in [i], the presence of implanted Br atoms in the E-series did not significantly influence the lifetime or the mobility.

3.2 Microcrystalline silicon

Microcrystalline silicon is a complex semiconductor material, which drives attention of the companies producing solar cells, displays and other opto-electronics devices. It consists of large microcrystalline Si grains (hundreds of micrometers) embedded in amorphous Si tissue (see Fig. 3.1). Large grains consist of small grains with dimensions of ∼20 nm. Both, the amorphous and the microcrystalline phase, can absorb different parts of the solar radiation, so the thin-film microcrystalline solar cells are more efficient than the pure thin-film amorphous Si solar cells. Their another advantage over amorphous Si cells is that they do not degrade in time. On the other hand, if produced in large numbers, they could be an interesting alternative to solar cell produced from expensive monocrystalline Si ingots, where the cutting and polishing of the ingots to a solar cell causes considerable loss of material. Moreover, microcrystalline solar cells can have thickness only in the orders of microns, which is sufficient for the efficient absorption of the solar energy, if advanced light trapping mechanisms are used. In addition, they can be deposited on cheap glass or plastic substrates.

The exact structure of the thin films of microcrystalline silicon can vary dramatically with different deposition conditions (for example size and nucleation density of the large grains or the thickness of the amorphous incubation layer). We have studied four ≈ 1μm thick samples prepared by PECVD method in department of Thin Films, from which was one amorphous and three were microcrystalline; the microcrystalline samples differ in crystallinity (20, 52, 72 % - bulk; 62, 75, 80 % - surface) and in the diameter of large grains (720, 470, 280 nm).

In contrast to InP, where the interband transport of carriers is observed and main results are DC mobilities and the lifetime of carriers, in microcrystalline silicon the mech-

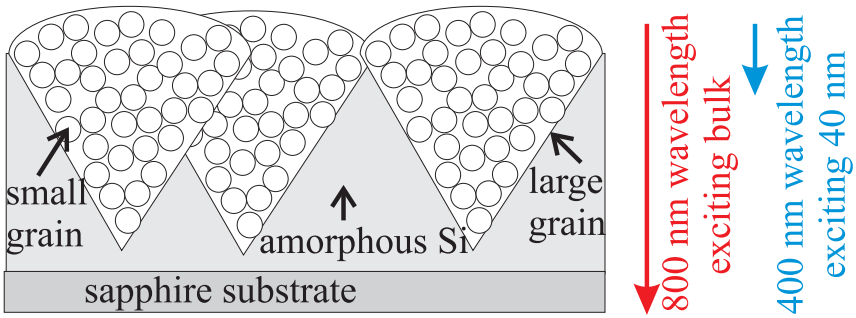

Figure 3.1: Scheme of a microcrystalline sample on a Sapphire substrate: Large grains (∼ hundred nanometers) have conical shape with a cap. They consist of small grains (∼ 20 nm). Large grains are surrounded by amorphous tissue. Small grains are assumed to be closely packed

anisms of the transport, characterized by the dispersion of mobility in the THz range and spectral marks of the localization of carriers, were studied.

To study mechanisms of carrier transport we carried out optical-pump THz-probe experiments. The first measurements were done at room temperature and under 800 nm excitation [iii]. These measurements were followed by experiments with 400 nm excitation at room temperature and experiments at cryogenic temperatures (150, 100, 20 K) with both excitation wavelengths [ii]. We exploited the different excitation wavelengths in order to study either the carrier response averaged over the entire film (800 nm excitation) or coming from the 40 nm surface layer (400 nm excitation), respectively.

The first results revealed that there are two different timescales of the dynamics in these samples. The pump-probe scans, which represent an overall THz response are presented in Fig. 3.2 (800 nm and 400 nm excitation). The first is ultrashort ($\approx$ 0.6 ps), and the second is much longer ($\approx$ 0.6 ns). The second component for 400 nm excitation was found to be 2-3 times faster due to the capture of carriers in localized surface states.

The first component was studied using the collinear experimental setups showed in Fig. 2.2b,c introduced in Section 2.2, where the normal incidence of the THz and the pumping beams provides the ultimate time resolution. To describe processes which may be faster than the length of the probing THz pulse a set of transient wave forms $\Delta E(\tau, \tau_p)$ is measured for several pump-probe delays and a dense 2D grid of data is obtained. The data are subsequently transformed using Fourier transformation to ω, ω_p space and the photoinduced conductivity $\Delta\sigma(\omega, \omega_p)$ is analyzed by models introduced in Sec 2.4 or their combination. An example of an analysis of data in the 2D Fourier space is presented in Fig. 6 in [ii].

The type of behavior of all microcrystalline samples was found to be very similar

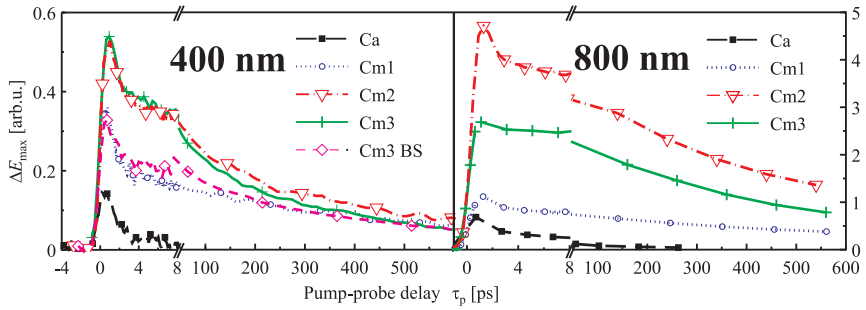

Figure 3.2: Pump-probe scans: maximum field amplitude of the transient THz signal ($\Delta E_{\max}(\tau_p)$) versus pump-probe delay for samples excited at 400 nm and 800 nm at the room temperature. The Ca symbol represents the amorphous sample, Cm1 is the least crystalline sample and Cm3 denotes the most crystalline sample. The curve named Cm3BS represents the sample Cm3 excited from the back-side (through the sapphire substrate).

during the the first 1 ps (at room temperature using photoexcitation with both excitation wavelengths). This ultrafast dynamics could be ascribed to free hot carriers with a mobility of $\sim 70\text{cm}^2/\text{Vs}$. From their mobilities we have evaluated the diffusion length $l_D \sim 17$ nm, which delimits the distance through which the electrons can travel prior to their relaxation to states with much lower mobility and found out that l_D is very similar to the size of the small grains. Based on this fact, we concluded that after 0.6 ps these hot carriers are trapped in the states located at the small-grain boundaries.

The analysis of the slower sub-picosecond component is based on the evaluation of photoinduced conductivity $\Delta\sigma(\omega, \tau_p)$ measured for several (typically 4-7) pump-probe delays. As the dynamics here evolves on a much longer scale than the length of the probing THz pulse, the quasi-static approach introduced in Sec. 2.3.3 can be used.

All investigated microcrystalline conductivity spectra exhibit an increase of the mobility with increasing frequency. This implies the response of localized carriers. We proposed two models describing the response of electrons in these localized states during the second sub-nanosecond part. The first model, introduced in [iii], characterized the photoinduced conductivity $\Delta\sigma$ as a sum of three contributions: one from the free carriers (described by the Drude term as in Eq. 2.23) and two from the localized carriers (described by the Debye relaxators as in Eq. 2.24).

Although the model was able to describe all measured data, its results were not compatible with expected results for the temperature measurements and with the generally accepted idea of small energetic barriers between small microcrystalline grains which would lead to only a small localization of carriers (for more details see the Fig. 8. in [ii] and discussion below it).

The second model was based on the description of electrons by a hopping conduction (see Sec. 2.3.6). The hopping model was able to describe measured data with a similar quality of the fit as the previous model. The typical photoinduced conductivity spectra for amorphous and microcrystalline sample are presented in Fig. 3 in [ii]. In the case of the amorphous sample we observed the saturation of the hopping at ~ 1 THz, with the hopping limited by the disorder in the amorphous tissue. On the other hand, in the microcrystalline type of spectra the saturation of the conductivity occurs at higher frequencies, which are not directly experimentally accessible. This behavior is inferred only from an extrapolation of our data in the fitting curves. Therefore the values of the cut-off frequency are less precise and serve only as rough estimations.

The cut-off frequency for the most crystalline samples was evaluated from the fits to be ~ 10 THz at room temperature. Upon cooling from 300 to 20 K the photoinduced conductivity exhibited quantitatively the same behavior for all samples, which implies that the carrier transport mechanisms do not change with temperature. However, in microcrystalline samples, the cut-off frequency shifts to higher frequencies at low temperatures. For example for the most microcrystalline samples the cut-off frequency at 20 K shifted to 22 THz. The difference between the slope of the photoinduced conductivity at 300 K and at 20 K in a microcrystalline sample can be clearly seen in Fig. 5 in [ii]. This

suggests that the hopping of carriers is hindered by scattering mechanisms, which limits the upper hopping frequency and the maximum hopping conductivity; the experimental results suggest that these mechanisms may become less efficient at low temperatures in microcrystalline samples.

The explanation could be found in the presence of the LO phonon in silicon at 16 THz, where at room temperature the phonon is populated and its interaction with photogenerated carriers influences the position of the cut-of frequency. On the contrary, at low temperature when the phonon states are not populated, the saturation is systematically observed at higher frequency.

In experiments with 400 nm excitation, where only a thin 40-nm-thick top (or eventually bottom) layer is studied, but where a much higher carrier concentration was generated, the values of the mobility were systematically about 3 to 5 times lower than those obtained for 800 nm. This suggests that the carrier-carrier scattering mechanisms strongly influence the transport.

Finally, at room temperature after $\approx$ 700 ps (800nm excitation) and $\approx$ 400 ps (400 nm excitation) photogenerated carriers became trapped in deeper localized states at grain boundaries of large grains and therefore became invisible for THz radiation.

3.3 Active optical control of the THz reflectivity of high-resistivity semiconductors

In this part of the thesis an idea of the optically controlled modulation of THz radiation using photoexcited carriers in a semiconductor material will be deployed. Most experiments were performed on GaAs, which is known for its high mobility of carriers and possible ultrafast (picosecond to subpicosecond) carrier lifetime (LT-GaAs). Moreover, GaAs can be efficiently photoexcited by the 800 nm radiation available in our laboratory.

Generally, opto-THz modulators are devices in which the information from the optical spectral band can be transformed to the THz one. In our case, the material which allows the transformation is a semiconductor. Semiconductors are in their steady-state transparent for THz radiation. However, if a semiconductor is photoexcited, free carriers, generated within the penetration depth for the excitation wavelength, strongly interact with THz radiation. This phenomenon can be used for blocking or reflecting the THz signal. The strength of the interaction between THz radiation and photoexcited carriers in a semiconductor can be tuned by the intensity of optical excitation.

In the first stage of our work we focused on the experimental verification of our method and we studied internal reflection on a photoexcited layer in a GaAs wafer [iv]. In the second stage of our work we concentrated our effort on decreasing the optical power necessary to obtain significant modulation of the THz beam. This was achieved by encapsulating the GaAs wafer in a resonant structure similar to a Fabry-Perot resonator [v], [vi].

3.3.1 GaAs wafer modulator

The scheme used in the first type of experiments is shown in Fig. 3.3. We have modified the strength of the interaction in the photoexcited layer by creating carrier concentrations between $\approx 10^{16}$ and 10^{19}cm^{-3}, and its thickness by using 800 and 400 nm excitation wavelengths. The THz pulse was reflected from the inner side of the semiconductor at the air/excited semiconductor/unexcited semiconductor interface. The unique scheme of our experiment allowed us to measure the reflectivity of the photoexcited layer in a standard transmission THz setup. The principle of this scheme and the pathway of the optical and THz pulses in the GaAs wafer is shown in Fig. 3.3. For probing the photoexcited layer we used the part of the THz pulse (E_1 first echo) which was reflected at the back side of the GaAs wafer. The transmitted part E_0 of the pulse was used as a reference. After the Fourier transformation of the waveforms of pulses E_0 and E_1 the complex amplitude reflectance spectrum of the photoexcited surface can be evaluated as

$$r(\omega) = \frac{E_1(\omega)}{r_0 E_0(\omega)} \tag{3.1}$$

where r_0 is the amplitude reflection coefficient of the unexcited GaAs surface.

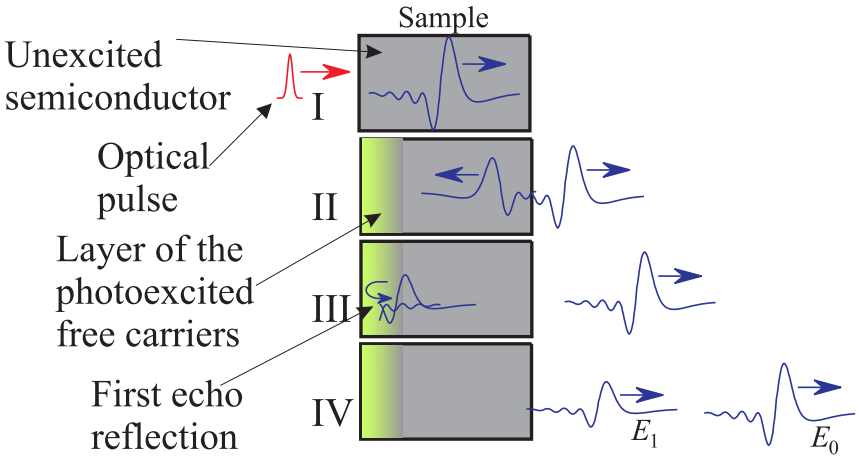

Figure 3.3: Scheme of the experiments performed on a broad-band opto-THz modulator: I: The THz pulse arrives before the excitation pulse so it propagates through the unexcited semiconductor wafer. II: The optical pulse generates a layer of photoexcitated carriers at the front side of the wafer. In the meanwhile THz pulse partially reflects at the back side. E_1- the first echo will probe the photoexcited layer from inner side. III: The THz pulse is reflected at the air/excited-semiconductor/unexcited-semiconductor interface. IV: The transmitted part of the THz pulse E_0 and the reflected first echo E_1 leave the semiconductor wafer

The THz reflection from the photoexcited surface strongly depends on the the excitation intensity. If the excitation intensity is high a thick layer of photoexcited carriers, which acts as a mirror for THz radiation, is created at the front surface of the semiconductor. On the other hand, in the case of the excitation at moderate intensity levels an interference occurs between partial waves reflected at the inhomogeneous interface. For specific narrow range of pump intensities this interference is destructive and the inner reflection of the THz pulse is significantly diminished.

In a quantitative description of the system, the carrier concentration in the photoexcited thin film can be characterized by the exponential decrease of the carriers along the surface normal implying a smooth change of the refractive index. The spectrum of the complex refractive index of the photoexcited layer can be evaluated from the Drude model:

$$N(z,\omega) = \sqrt{\epsilon_\infty + \sum_{i=n,e} \frac{N_d(z) e_0^2}{\epsilon_0 m_i} \left[\frac{1}{-\mathrm{i}\omega/\tau_i - \omega^2} \right]}; \qquad N_d(z) = N_d(0) e^{-\alpha z} \tag{3.2}$$

where ϵ_∞ is the high-frequency permittivity, ϵ_0 is the vacuum permittivity, m_i is the mass of the photogenerated carriers with scattering times τ_i, N_d is the carrier concentration, α is the absorption coefficient and ω is the angular frequency. Finally, the reflectance can be evaluated using transfer matrix formalisms in inhomogeneous media [100].

The dependence of the power reflectance on the carrier concentration (incident optical pump fluence) is shown in Fig. 2 in [iv]. For 800 nm excitation we were able to adjust the power reflectance of THz radiation from 3% in the antireflective regime (using pump fluence ≈ 5.4 μJ/cm^2 creating $\approx 10^{17}$cm^{-3} carriers) to a highly-reflective regime with 85 % of power reflectance (using pump fluence ≈ 200 μJ/cm^2 creating $\approx 10^{19}$cm^{-3} carriers).

In the case of the 400 nm excitation the reflectance curve is shifted to higher carrier concentrations by approximately two orders of magnitude with respect to that for the 800 nm excitation. This fact is caused by a higher absorption coefficient for the 400 nm excitation, which is responsible for a much thinner photoexcited layer (~ 17 nm). With optical pump fluences of ≈ 100 μJ/cm^2 we were able to obtain only the antireflective regime.

In addition, the amplitude of the THz wave reflected on the structure under investigation is closely related to the phase change. The wave exhibits a $\pi/2$-shift upon reflection under antireflecting conditions and a change of the sign (π-shift) in the high-reflectivity regime, so the device can work also as a phase shifter. The clear difference of the phase in waveforms reflected on the photoexcited layer in different stages of the reflectance curve is shown in Fig.1 in [iv]. The dependence of the phase shift on the carrier concentration is presented in Fig. 2 in [iv].

For the highest pump fluences $\phi \gtrsim 70\mu\mathrm{Jcm}^{-2}$ the shift of the phase reaches values clearly below $-\pi$. Also measured points of the reflectance do not follow the theoretical curve. This discrepancy is caused by non-linear effects, such as two photon absorption or saturation of single-photon absorption, which were not included in our model [101].

The same phenomena can be studied also in other semiconductors. However, for example in silicon, where the lifetime of the carriers is much longer compared to GaAs, the diffusion of carriers plays a significant role. Because of the diffusion a thick layer of photoexcited carriers with a slowly varying carrier density builds up. In this case the efficient absorption of THz radiation in the layer prevents from achieving the reflective regime. As we suggested, a thin film layer of silicon (4 μm) on an insulating transparent substrate would suppress the diffusion and simultaneously define the thickness of the photoexcited layer (see Fig. 3 in [iv]).

3.3.2 Photonic-crystal opto-THz modulator

In the previous paragraph we have described a device where a broad spectral range of THz radiation could be modulated simultaneously. The drawback of this approach was that to control the reflectivity of the GaAs-wafer device relatively high concentrations of carriers ($10^{17} - 10^{18}\mathrm{cm}^{-3}$) produced by intense pulses were necessary. Such intense pulses could be produced only by an amplified laser system. Our aim was therefore focused on finding a possibility to decease the excitation energy needed for the modulation to levels achievable by femtosecond oscillators. This would allow for a significant reduction of the costs of a system equipped with such a device. This goal could be achieved by encapsulating a thin GaAs wafer into a 1 dimensional photonic-crystal (PC). As the investigated structure has a resonant character, it shows a narrower operation bandwidth, which makes it suitable for applications with quasi-monochromatic THz radiation. Simultaneously, due to the THz electromagnetic field enhancement in the GaAs layer, this device allows one to modulate efficiently the THz light at substantially lower photoexcitation fluences, while the speed of the switching is determined by the lifetime of the carriers at the surface of the GaAs wafer.

The device can be described as a PC with a defect in the middle made of the semiconductor slab (see Fig. 3.4). The structure of the PC consists of quarter-wave stacks of alternating materials with high (H) an low (L) refractive indices, which are simultaneously transparent for both THz and pump radiation. A band-gap of forbidden frequencies, where the transmission through the structure is significantly reduced, forms in the THz range. The central GaAs half-wave plate introduces a defect mode which is situated in the middle of the forbidden band. The transmission of the PC at the frequency of the defect mode is controlled by the photoexcitation of the surface of the semiconductor, where the relatively high transmission in steady state can be significantly reduced due to the interaction of pohotoexcited carriers with the THz field. The device can be understood as a Fabry-Perot interferometer consisting of two identical thick Bragg mirrors enclosing a cavity made of GaAs semiconductor.

Mathematically, the structure can be described as a multilayer. One of the most convenient descriptions of layered structures is the transfer matrix formalism, where each layer is characterized by a matrix which connects the tangential components of the electric

and magnetic field at the input and output interface of the layer [68], [102]. The transfer matrix of the whole multi-layer stack equals the product of the transfer matrices of all its constituents.

In our case, the PC was divided into three blocks P, S and Q (see Fig. 3.4). Blocks P and Q are in fact identical Bragg mirrors where the order of H and L layers is reversed; the S layer represents the semiconductor. The complex THz refractive index of photoexcited GaAs of the S-block is evaluated using the Drude model.

There are four possible configurations of a symmetrical PC which differ in the structure of the P and Q blocks. The identical Bragg mirrors P and Q are formed by a sequence of bilayers of materials with high and low indices; each of the border layer can be either low- or high- index material. The Q-block is constructed symmetrically with respect to the P-block. We have theoretically investigated the following structures:
(1) the block P is LHLHLHLHL (the structure is abbreviated as LHL);
(2) P is HLHLHLHL (abbrev. HL);
(3) P is LHLHLHLH (abbrev. LH);
(4) P is HLHLHLHLH (abbrev. HLH).
In the case of the asymmetrical PC structures the transmittance at the defect mode in the steady state is significantly reduced in comparison to the symmetrical structure, this makes such structures less interesting from the point of view of possible applications.

Let us denote by r_P and t_P the THz field reflectance and transmittance of the block P surrounded by air and by r_{SQ} and t_{SQ} the field reflectance and transmittance of the block SQ in air (for more details see Fig. 3.4). Considering the assumptions that the penetration depth of the photoexcited layer of the semiconductor is small in comparison

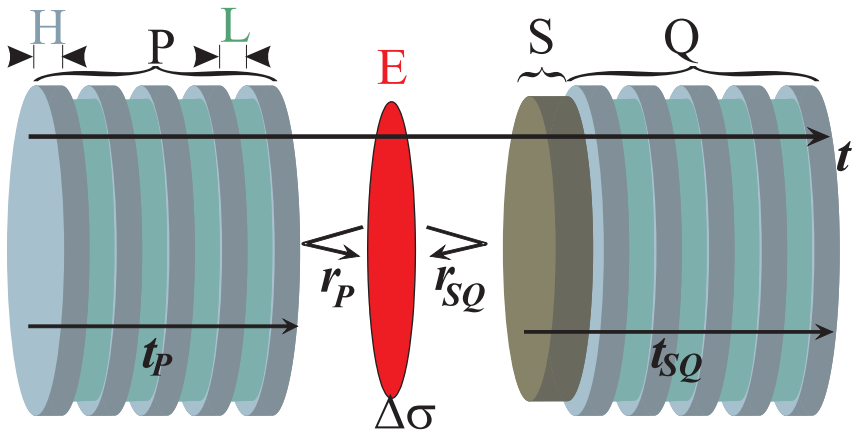

Figure 3.4: Scheme of the PC-modulator: Blocks P and Q (Bragg mirrors) consist of alternating slabs of material with high (H) and low (L) indices. S block is the GaAs semiconductor slab with a photoexcited layer E.

to its thickness and to the THz wavelength and that the response of the photonic structure (defined by τ_{PC} - see below) is faster that the carrier lifetime (τ_{C}) in the semiconductor, the dynamical response of the PC to the photoexcitation can be written in a form [vi]:

$$\Delta E_t(\omega, \tau_p) = -\frac{\eta_0}{2\alpha}\, U_P(\omega)\, t(\omega)\, U_{SQ}(\omega)\, t(\omega)\, \Delta\sigma(\omega, \tau_p) E_{\mathrm{inc}}(\omega)\,, \tag{3.3}$$

where η_0 is the impedance of the vacuum, α is the absorption coefficient of GaAs at 800 nm, $\Delta\sigma$ is the photoexcited conductivity of the semiconductor and E_{inc} is the incident THz field. The transmission function t of the whole PC is small in the entire forbidden band except for a narrow range around the defect mode frequency ω_0. The enhancement factors U_P and U_{SQ} can be evaluated from the corresponding field reflectances r_{SQ} and t_{SQ}:

$$U_P(\omega) = \frac{1 + r_P(\omega)}{t_P(\omega)}\,, \qquad U_{SQ}(\omega) = \frac{1 + r_{SQ}(\omega)}{t_{SQ}(\omega)}\,. \tag{3.4}$$

The transmission functions of the blocks t_{SQ} and t_P exhibit a forbidden band without the defect mode. The reflectances r_{SQ} and r_P reach values close to either -1 or 1 inside the forbidden band near the defect mode frequency. Consequently, the enhancement factors may reach values either significantly higher than 1 or smaller then 1 making the structure either sensitive or insensitive to the photoexcitation. The enhancement factors for the studied structures are shown in Fig. 2 in [vi].

If an L layer is adjacent to the defect (LHL and HL structures), the reflectances r_P and r_{SQ} reach values ≈ 1, leading to high value of enhancement factors. In our situation, when the optical thickness of the defect in the THz range is a half-wave plate, the defect mode (the electric-field of the standing waves inside the structure) in the center of the forbidden band exhibits an odd symmetry, which results in anti-nodes at the edges of the defect (see Fig. 2b in [vi]) leading to the strong enhancement of the opto-THz modulation.

In contrast, if the H layer is adjacent to the defect layer, the electric-field of the standing waves exhibit nodes at the surface of GaAs (the defect mode has an even symmetry). This corresponds to small values of the enhancement factors at the edges of the defect layer which makes the structures HLH and LH not suitable for opto-THz modulation. The character of the defect mode in dependence of the thickness of the defect layer for LHL and HL structure can be found in Fig. 3 in [vi].

Another factor which is strongly correlated to the magnitude of the enhancement factors is the strength of the electric-field localization. This characteristics depends on the number of periods of the Bragg mirrors and on the nature of the outermost layers of the PC. A higher number of bilayers leads to higher quality of the Bragg mirrors, implying better field localization. Moreover, if the outermost layer is the H layer the higher impedance mismatch between the structure and air can significantly increase the field enhancement.

However, the localization of the field at the defect layer and the dynamical response of the structure are tightly connected together. The most important parameter which defines the speed of the device here is the lifetime τ_{PC}. It can be interpreted as the lifetime of the

THz wave inside the resonator and it can be easily shown that $\tau_{\mathrm{PC}} = 1/\pi\Delta f$, where Δf is the full-width-at-half-maximum (FWHM) of the defect mode frequency f_0. For example, the HL structure with the highest field localization at the photoexcited layer (small Δf) and therefore the best performance for the optical control of the THz propagation will exhibit slower response than the LHL structure. A compromise thus should be found between the speed of the device and enhancement of the electric field.

As the results of the calculations showed that LH and HLH structures are not sensitive to the photoexcitation (see Fig. 4 in [vi]), we built two symmetrical PCs with LHL and HL design of the Bragg mirrors for our experiments. In both these cases the L layer is the layer adjacent to the defect. The scheme of the LHL structure is shown in Fig. 3.5. The defect layer was made of optically polished weakly chromium-doped GaAs. The photoexcited carriers in the GaAs wafer exhibited Drude-like behavior with the carrier lifetime $\tau_C = 170$ ps and the scattering time $\tau_S = 160$ fs (see Fig. 8 in [vi]). The thicknesses of all layers were chosen according to theoretical predictions in order to obtain the defect mode frequency in the middle of the forbidden band (at 609 GHz for the LHL structure and 606 GHz for the HL structure). The modulation of the amplitude transmission at several pump fluences for both structures is presented in Fig. 9 in [vi]. At the pump fluence of $0.4\mu\mathrm{J/cm}^2$ the carrier concentration of $10^{16}\mathrm{cm}^{-3}$ was achieved. With this pump fluence the ratio T/T_0 between the power transmission of the PCs in the photoexcited and ground states at the defect mode frequency f_0 was 0.4 for the HL structure and 0.6 for the LHL structure (for full information about the variation of the transmitted power at the defect mode frequency as a function of the pump fluence and/or free carrier concentration see Fig. 10c in [vi]).

The time response of our PCs depends on both τ_{PC} and the lifetime τ_{C} of free electrons in GaAs. In the case of the modulation of a monochromatic THz wave the PC-resonator in its ground state dynamically stores a part of THz electromagnetic energy. At the photoexcitation event the input port is made opaque and the stored energy is depleted with the lifetime τ_{PC} (switch-on time of the modulator). The high transmission of the structure

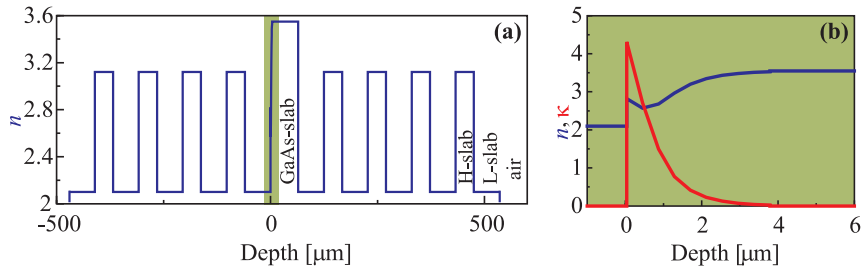

Figure 3.5: (a) Scheme of the refractive indices and thicknesses of particular layers of the LHL structure. (b) Detail of the depth profile of the refractive index in the photoexcited GaAs wafer.

is restored with the lifetime τ_C (switch-off time of the modulation). The modulation pulse with initial decrease due to τ_{PC} and a restoration with τ_C can be seen in Fig. 7 in [vi]. The time response of the PC can be defined as the width at one half of pulse modulation maximum. The magnitude of the modulation depends on the ratio τ_{PC}/τ_C. If $\tau_C < \tau_{PC}$ the modulation depth is significantly reduced. For example the theoretical response time curves for semiconductors with different carrier lifetimes are shown in Fig. 7b in [vi]. A PC with an LHL structure and a defect made of a semiconductor with carrier lifetimes of 10 ps would exhibit ultrafast response, however, the power modulation would be very small (20%). The time response of our modulators was found to be faster than 330 ps for the HL structure (exhibiting τ_{PC} = 60 ps) and 200 ps for the LHL structure (with τ_{PC} = 18.5 ps). Nevertheless, the pump pulse energies necessary to induce a 50% modulation of the THz power are comparable to those delivered by current commercial femtosecond oscillators. The bit rate of these elements is then determined by the femtosecond oscillator repetition rate.

Following our estimations (based on a very good agreement between the theory and experiments in the available structures) in a semiconductor with the carrier lifetime 70 ps and an LHL-Bragg-mirror structure 100-ps-long modulation with 42% modulation depth of the THz output power could be achieved when the PC is photoexcited by commercially available femtosecond oscillator system (creating the carrier concentration of $^{1}0^{16}\mathrm{cm}^{-3}$).

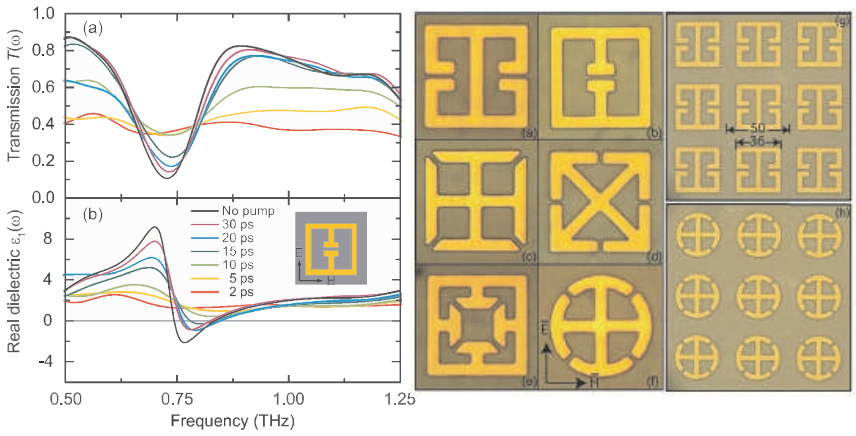

Figure 3.6: Left panel: Frequency-dependent transmission of the eSRR array at various times following photoexcitation and corresponding real part of the effective dielectric function. Inset, metamaterial eSRR unit cell; arrows, polarization of the normally incident THz radiation (Fig. taken from [103]). Right panel: Different shapes of eSRRs with a example of a metamaterials pattern.

A terahertz-modulator with comparable properties, but working on very different principle was introduced by Chen et al. [103]. As this is, to our knowledge, the only comparable

opto-THz switch in the literature, it is worth looking in more detail at this structure to yield comparison. They demonstrated optical switching of electrically resonant terahertz planar metamaterials fabricated on ErAs/GaAs nanoisland superlattice substrates. The metamaterial consisted of periodically patterned split ring resonators (SRRs) which displayed a strong resonant electromagnetic response. Importantly, the resonant frequency can be scaled with the SRR dimensions [104] or the resonant frequency can be given by the unit cell [105].

With the unit cell having an outer dimension of 36 μm, a lattice parameter of 50 μm, a linewidth of 4 μm, and a gap of 2 μm and the shape two letters C (facing each other) the material had a resonance at 0.75 THz (see Fig. 3.6). The substrate, made of a ErAs/GaAs superlattice structure grown by molecular beam epitaxy on an intrinsic GaAs wafer (20 periods with L=100 nm), was designed to shorten the carrier recombination time to 10 ps. The charge carriers generated during the photoexcitation event shunt the capacitive regions of the constituent elements, thereby modulating the resonant response of the metamaterials. A switching recovery time of 20 ps results from fast carrier recombination in the ErAs/GaAs superlattice substrates. To shunt the resonant response a fluence of $\sim 1\mu J/cm^2$ (corresponding to carrier density of $10^{16}cm^{-3}$) was used. The switching was demonstrated between values of transmittance 0.1 (steady-state) 0.35 (photoexcitated-state) and in a complementary structure between 0.35 (steady-state) and 0.1 (photoexcitated-state).

Compared to our device, this device has 2.5 times higher power requirements, but is approximately an order of magnitude faster. However, our device is much simpler from the point of view of fabrication. An advantage of our device can be also found in the transmission close to 1 in the steady state.

3.4 Outlook

Our future plans consist on the one hand in a new concept of the broad-band opto-THz modulator, which will be built of a semiconductor wafer attached to a prism. The THz pulse will be led through the prism towards the photoexcited semiconductor wafer, where, because of higher refractive of the prism compared to air, the THz pulse could be better focused than in air and consequently lower excitation intensities could be used to achieve the high reflection regime (unamplified femtosecond laser system).

On the other hand, the research of ultrafast semiconductors still continues. In near future an ultrafast semiconductor material $In_{0.53}Ga_{0.47}As$ (InGaAs) will be studied in our laboratory. This material draws attention due to its bandgap, which allows for the photoexcitation by the compact, low-cost and stable fiber lasers operating at 1.5 μm frequency. By the high-energy (11 MeV) heavy-ion-irradiation technique, the bombardment with Br^+ ions (irradiation doses may reach values from 10^9 to 10^{12} cm^{-2}) mainly produces only massive atom displacements at the surface region of the sample. The samples will consist of initially undoped 3μm-thick InGaAs layers epitaxially grown by the molecular-beam epitaxy (MBE) method on semi-insulating InP:Fe substrates. Due to the very high initial energy of the Br ions, the irradiating ions will be implanted rather deep in the InP substrate just beyond the 3 μm InGaAs layer thus they should not influence parameters of the studied InGaAs samples. In this material the ultrafast dynamics dependant on the dose of the ion-bombardment will be studied.

3.5 Summary

The thesis is focused on two topics. The first one is based on the investigation of photoexcited carriers in semiconductors (thin-film microcrystalline silicon, InP) and their properties on the sub-picosecond to nanosecond timescale in the THz spectral range. The second topic covers research of the modulation of the THz-pulse reflection on the photoexcited semiconductor layer and the modulation of the transmittance through a device (modulator) made of a photonic-crystal with a defect formed by a semiconductor wafer. In both cases the modulation was controlled by the photoexcitation intensity. The main original contribution of the thesis consists in several results, most of them having been published or accepted for publication in international peer-reviewed journals (see the Appendix). Each of them is here concluded separately and the emphasis is put on the author's contribution:

1. Using the time-resolved THz spectroscopy method (TRTS) we studied InP semiconductor, which was subject to a high energy (11 MeV) heavy-ion (Br^+) bombardment [i]. The bombardment induces host atom displacements near the wafer surface, while ions used for the bombardment are implanted a few microns below the wafer surface. At a high bombardment dose the carrier lifetime was severely reduced down to 290 fs. The response of the carriers was successfully characterized by the Drude model. We found the influence of the dose of the bombardment to be inversely proportional to the mobility of carriers; the mobility dropped from initial $\mu = 3000$ cm^2/Vs (as-grown sample) to $\mu = 900$ cm^2/Vs for the most bombarded one. Finally, a model of carrier dynamics including the carrier trapping, trap filling and carrier diffusion was developed to gain a deeper insight into electron and hole dynamics. This allowed us to extract the density of traps along with electron and hole lifetimes in selected samples.

In particular, the author's contribution to this topic consists in assembling an upgrade of the THz experimental setup for the measurement of the ultrafast subpicosecond dynamics, the measurement of all TRTS data and in a large part to the evaluation of sub-ps and sub-ns conductivities, mobilities and time decays of the carriers.

2. We performed TRTS measurements on a set of thin-film microcrystalline silicon samples, with structures varying from amorphous to fully microcrystalline [iii], [ii]. The samples were excited at 800 and 400 nm; this allowed us to obtain an averaged response over the whole film thickness in the former case and the response from the 40-nm-thick photoexcited surface layer in the later case. Moreover, we studied the samples at temperatures down to 20 K. The nanoscopic electrical transport properties markedly changed on a sub-picosecond time scale. While the initial transient photoconductivity of the samples was dominated by hot free carriers with a mobility of $\mu = 70$ cm^2/Vs, which were after 0.6 ps trapped into weakly localized hopping states, the response at the nanosecond timescale was found to be dominated by

the hopping process. Following our experiments the low-frequency mobility of the observed hopping process is of the order of 20 cm^2/Vs. In microcrystalline samples the hopping was found to be influenced by electron-phonon interaction. In the amorphous sample the factor limiting the hopping was attributed to the disorder in the material. This work involves a huge set of experimental data and significantly contributes to the understanding of the transport mechanisms in microcrystalline silicon.

The author's contribution to this part consists namely in the measurement of all TRTS data (all temperatures, both excitation wavelengths) and Raman measurements (the evaluation of the crystallinity of the samples). Moreover, the author performed the retrieval of all sub-picosecond-scale and nanosecond-scale parameters of dynamics and significantly contributed to the final interpretation of the global set of the data.

3. We have studied the internal reflectivity of the THz pulse on a photoexcitated layer of carriers generated on a surface of a GaAs wafer by amplified femtosecond laser pulses [iv]. We succeeded in tuning the THz reflectivity accordingly to the intensity of the photoexcitation. The reflection occurred inside the GaAs wafer on an inhomogeneous photoexcitated layer, where, at moderate pump intensities, a destructive interference was found to be responsible for a very low power reflectance coefficient ($R < 3\%$). At high pump intensities (carrier concentrations of $10^{18} - 10^{19}cm^{-3}$), the power reflectance coefficient reached the value of $R > 85\%$. This strong modulation of the THz reflectivity was observed in a broad range of THz frequencies (0.5 - 1.5 THz).

The experience gained in the previous research on a broad-band THz modulator were utilized in the fabrication of a photonic-crystal narrow-band THz modulator [v], [vi]. The modulator was composed of a photonic-crystal with a defect layer made of a GaAs semiconductor platelet. The transmission at the defect mode frequency was modulated by optical pump intensities achievable by a femtosecond oscillator. Four different symmetrical resonant structures were theoretically studied, from which two optimal ones were constructed and experimentally studied. The dynamical response of these elements was shown to be controlled by the lifetime of THz photons in the resonator and by the free carrier lifetime. The time response of the studied structures is shorter than 330 ps.

The author has measured all TRTS data and evaluated the corresponding reflectivities and transmittances data. The author has also participated on the simulation of the studied structures and contributed to the design optimization and data interpretation.

References

[1] C. Fattinger and D. Grischkowsky. Terahertz beams. *Appl. Phys. Lett.* **54**, 490 (1989).

[2] D. H. Auston, K. P. Cheung, and P. R. Smith. Picosecond photoconducting Hertzian dipoles. *Appl. Phys. Lett.* **45**, 284 (1984).

[3] F. E. Doany, D. Grischkowsky, and C. C. Chi. Carrier lifetime versus ion-implantation dose in silicon on sapphire. *Appl. Phys. Lett.* **50**, 460 (1987).

[4] H. Němec, F. Kadlec, C. Kadlec, P. Kužel, and P. Jungwirth. Ultrafast far-infrared dynamics probed by terahertz pulses: A frequency domain approach. II. Applications. *J. Chem. Phys.* **122**, 10 4504 (2005).

[5] M. van Exter, C. Fattinger, and D. Grischkowsky. High brightness terahertz beams with an ultrafast detector. *Appl. Phys. Lett.* **55**, 337 (1989).

[6] R. W. Ziolkowski and J. B. Judkins. Propagation characteristics of ultrawide-bandwidth pulsed Gaussian beams. *J. Opt. Soc. Am. A* **9**, 2021 (1992).

[7] P. K. Benicewicz and A. J. Taylor. Scaling of terahertz radiation from large-aperture biased InP photoconductors. *Opt. Lett.* **18**, 1332 (1993).

[8] A. Dreyhaupt, S. Winnerl, T. Dekorsy, and M. Helm. High-intensity terahertz radiation from a microstructured large-area photoconductor. *Appl. Phys. Lett.* **86**, 12 1114 (2005).

[9] R. Adamovičius, G. Molis, A. Krotkus, and V. Sirutkaitis. Spectral dependencies of terahertz emission from InAs and InSb. *Appl. Phys. Lett.* **87**, 26 1101 (2005).

[10] X.-C. Zhang and D. H. Auston. Optoelectronic measurement of semiconductor surfaces and interfaces with femtosecond optics. *J. Appl. Phys.* **71**, 326 (1992).

[11] M. Bass, P. A. Franken, J. F. Ward, and G. Weinreich. Optical rectification. *Phys. Rev. Lett.* **9**, 446 (1962).

[12] X.-C. Zhang, Y. Jin, K. Yang, and L. J. Schowalter. Resonant nonlinear susceptibility near the GaAs band gap. *Phys. Rev. Lett.* **69**, 2303 (1992).

[13] X.-C. Zhang, Y. Jin, and X. F. Ma. Coherent measurement of THz optical rectification from electro-optic crystals. *Appl. Phys. Lett.* **61**, 2764 (1992).

[14] A. Rice, Y. Jin, X. F. Ma, , X.-C. Zhang, D. Bliss, J. Larkin, and M. Alexander. Terahertz optical rectification from $\langle 110 \rangle$ zinc-blende crystals. *Appl. Phys. Lett.* **64**, 1324 (1994).

[15] A. Nahata, A. S. Weling, and T. F. Heinz. A wideband coherent terahertz spectroscopy system using optical rectification and electro-optic sampling. *Appl. Phys. Lett.* **69**, 2321 (1996).

[16] A. Schneider, M. Stillhart, and P. Günter. High efficiency generation and detection of terahertz pulses using laser pulses at telecommunication wavelengths. *Opt. Express* **14**, 5376 (2006).

[17] F. Kadlec, P. Kužel, and J.-L. Coutaz. Study of Terahertz Radiation Generated by Optical Rectification on Thin Gold Films. *Opt. Lett.* **76**, 1402 (2005).

[18] S. L. Chuang, S. Schmitt-Rink, B. I. Greene, P. N. Saeta, and A. F. J. Levi. Optical rectification at semiconductor surfaces. *Phys. Rev. Lett.* **68**, 102 (1992).

[19] D. H. Auston, K. P. Cheung, J. A. Valdmanis, and D. A. Kleinman. Cherenkov radiation from femtosecond optical pulses in electro-optic media. *Phys. Rev. Lett.* **53**, 1555 (1984).

[20] D. J. Cook and R. M. Hochstrasser. Intense terahertz pulses by four-wave rectification in air. *Opt. Lett.* **25**, 1210 (2000).

[21] M. Kress, T. Löffler, S. Eden, M. Thomson, and H. G. Roskos. Terahertz-pulse generation by photoionization of air with laser pulses composed of both fundamental and second-harmonic wave. *Opt. Lett.* **29**, 1120 (2004).

[22] Y.Chen, M. Yamaguchi, M. Wang, and X.-C. Zhang. Terahertz pulse generation from noble gases. *Appl. Phys. Lett.* **91**, 25 1116 (2007).

[23] T. Löffler, F. Jacob, and H. G. Roskos. Generation of terahertz pulses by photoionization of electrically biased air. *Appl. Phys. Lett.* **77**, 453 (2000).

[24] C. D. Amico, A. Houard, S. Akturk, Y. Liu, J. Bloas, M. Franco, B. Prade, A. Couairon, V. T. Tikhonchuk, and A. Mysyrowicz. Forward THz radiation emission by femtosecond filamentation in gases: theory and experiment. *New J. of Phys.* **10**, 01 3015 (2008).

[25] K. Kawase, J. Shikata, and H. Ito. Terahertz wave parametric source. *J. Appl. Phys.* **35**, R1 (2002).

[26] K. Kawase, Y. Ogawa, Y. Watanabe, and H. Inoue. Non-destructive terahertz imaging of illicit drugs using spectral fingerprints. *Opt. Express* **11**, 2549 (2003).

[27] K. Kawase, H. Minamide, K. Imai, J. Shikata, and H. Ito. Injection-seeded terahertz-wave parametric generator with wide tunability. *Appl. Phys. Lett.* **80** (2002).

[28] J. Faist, F. Capasso, D. L. Sivco, C. Sirtori, A. L. Hutchinson, and A. Y. Cho. Quantum cascade laser. *Science* **264**, 553 (1994).

[29] R. Köhler, A. Tredicucci, F. Beltram, H. E. Beere, E. H. Linfield, A. G. Davies, D. A. Ritchie, R. C. Iotti, and F. Rossi. Terahertz semiconductor-heterostructure laser. *Nature* **417**, 156 (2002).

[30] B. Williams. Terahertz quantum-cascade lasers. *Nat. Photon.* **1**, 517 (2007).

[31] C. Walther, M. Fischer, G. Scalari, R. Terazzi, N. Hoyler, and J. Faist. Quantum cascade lasers operating from 1.2 to 1.6 THz. *Appl. Phys. Lett.* **91**, 13 1122 (2007).

[32] M. Belkin, J. Fan, S. Hormoz, F. Capasso, S. Khanna, M. Lachab, A. Davies, and E. Linfield. Terahertz quantum cascade lasers with copper metal-metal waveguides operating up to 178 K. *Opt. Express* **16**, 3242 (2008).

[33] B. Williams, S. Kumar, Q. Hu, and J. Reno. Operation of terahertz quantum-cascade lasers at 164 K in pulsed mode and at 117 K in continuous-wave mode. *Opt. Express* **13**, 3331 (2005).

[34] A. Mohan, A. Wittmann, A. Hugi, S. Blaser, M. Giovannini, and J. Faist. Room-temperature continuous-wave operation of an external-cavity quantum cascade laser. *Opt. Express* **32**, 2792 (2007).

[35] B. Williams, S. Kumar, Q. Hu, and J. Reno. High-power terahertz quantum-cascade lasers. *El. Lett.* **42**, 89 (2006).

[36] A. Lyakh, C. Pflügl, L. Diehl, Q. J. Wang, F. Capasso, X. J. Wang, J. Y. Fan, T. Tanbun-Ek, R. Maulini, A. Tsekoun, R. Go, C. Kumar, and N. Patel. 1.6 W high wall plug efficiency, continuous-wave room temperature quantum cascade laser emitting at 4.6 μm. *Appl. Phys. Lett.* **92**, 11 1110 (2008).

[37] M. Belkin, F. Capasso, A. Belyanin, D. Sivco, A. Y. Cho, D. Oakley, C. Vineis, and G. Turner. Terahertz quantum-cascade-laser source based on intracavity difference-frequency generation. *Nat. Photon.* **1**, 288 (2007).

[38] M. A. Belkin, F. Capasso, F. Xie, A. Belyanin, M. Fischer, A. Wittmann, and J. Faist. Room temperature terahertz quantum cascade laser source based on intracavity difference-frequency generation. *Appl. Phys. Lett.* **92**, 20 1101 (2008).

[39] B. Gompf, M. Gerull, T. Müller, and M. Dressel. THz-micro-spectroscopy with backward-wave oscillators. *Infrared Phys. Techn.* **49**, 128 (2006).

[40] G. Grüner. *Millimeter and Submillimeter Wave Spectroscopy of Solids.* Springer-Verlag, Berlin, Heidelberg (1998).

[41] M. Abo-Bakr, J. Feikes, K. Holldack, P. Kuske, W. B. Peatman, U. Schade, G.Wüstefeld, and H.-W. Hübers. Brilliant, Coherent Far-Infrared (THz) Synchrotron Radiation. *Phys. Rev. Lett.* **90** (2003).

[42] G. L. Carr, M. C. Martin, W. R. McKinney, K. Jordan, G. R. Neil, and G. P. Williams. High-power terahertz radiation from relativistic electrons. *Nature* **420**, 153 (2002).

[43] L. Ozyuzer, A. E. Koshelev, C. Kurter, N. Gopalsami, Q. Li, M. Tachiki, K. Kadowaki, T. Yamamoto, H. Minami, H. Yamaguchi, T. Tachiki, K. E. Gray, W.-K. Kwok, and U. Welp. Emission of Coherent THz Radiation from Superconductors. *Science* **318**, 1291 (2007).

[44] E. J. Reed, M. R. Armstrong, K. Kim, M. Solja, R. Gee, J. H. Glownia, and J. D. Joannopoulos. Terahertz radiation from shocked materials. *Mater. Today* **10**, 44 (2007).

[45] S. Kono, M. Tani, P. Gu, and K. Sakai. Detection of up to 20 THz with a low-temperature-grown GaAs photoconductive antenna gated with 15 fs light pulses. *Appl. Phys. Lett.* **77**, 4104 (2000).

[46] H. J. Bakker, G. C. Cho, H. Kurz, Q. Wu, and X.-C. Zhang. Distortion of terahertz pulses in electro-optic sampling. *J. Opt. Soc. Am. B* **15**, 1795 (1998).

[47] Q. Wu and X.-C. Zhang. 7 terahertz broadband GaP electro-optic sensor. *Appl. Phys. Lett.* **70**, 1784 (1997).

[48] J. A. Riordan, F. G. Sun, Z. G. Lu, and X.-C. Zhang. Free-space transient magneto-optic sampling. *Appl. Phys. Lett.* **71**, 1452 (1997).

[49] A. Schneider, I. Biaggio, and P. Günter. Terahertz-induced lensing and its use for the detection of terahertz pulses in a birefringent crystal. *Appl. Phys. Lett.* **84**, 2229 (2004).

[50] W. L. Chan, J. Deibel, and D. M. Mittleman. Imaging with terahertz radiation. *Rep. Prog. Phys.* **70**, 1325 (2007).

[51] P. Kužel and F. Kadlec. Tunable structures and modulators for the THz light. *Comptes Rendus de l'Académie des Sciences – Physique* **9**, 197 (2008).

[52] E. Pickwell and V. P. Wallace. Biomedical applications of terahertz technology. *J. Phys. D: Appl. Phys.* **39**, R301 (2006).

[53] A. G. Davies, A. D. Burnett, W. Fan, E. H. Linfield, and J. E. Cunningham. Terahertz spectroscopy of explosives and drugs. *Mater. Today* **11**, 18 (2008).

[54] R. Appleby and H. B. Wallace. Standoff Detection of Weapons and Contraband in the 100 GHz to 1 THz Region. *IEEE Trans. Antennas Prop.* **55**, 2944 (2007).

[55] R. M. Woodward, B. E. Cole, V. P. Wallace, R. J. Pye, D. D. Arnone, E. H. Linfield, and M. Pepper. Terahertz pulse imaging in reflection geometry of human skin cancer and skin tissue. *Phys. Med. Biol.* **47**, 5853 (2002).

[56] P. Wallace, A. Fitzgerald, S. Shankar, N. Flanagan, R. Pye, J. Cluff, and D. Arnone. Terahertz pulsed imaging of basal cell carcinoma ex vivo and in vivo. *British J. Dermatol.* **151**, 424 (2004).

[57] E. Pickwell, V. P. Wallace, B. E. Cole, S. Ali, C. Longbottom, R. Lynch, and M. Pepper. A Comparison of Terahertz Pulsed Imaging with Transmission Microradiography for Depth Measurement of Enamel Demineralisation in vitro. *Caries Res.* **41**, 49 (2007).

[58] D. A. Crawley, C. Longbottom, B. E. Cole, C. M. Ciesla, D. Arnoneb, V. P. Wallace, and M. Pepper. Terahertz Pulse Imaging: A Pilot Study of Potential Applications in Dentistry. *Caries Res.* **37**, 252 (2003).

[59] Y. Morita, A. Dobroiu, C. Otani, and K. Kawase. A real-time inspection system using a terahertz technique to detect microleak defects in the seal of flexible plastic packages. *J. Food. Prot.* **68**, 833 (2005).

[60] Y.-C. Shen and P. Taday. Development and Application of Terahertz Pulsed Imaging for Nondestructive Inspection of Pharmaceutical Tablet. *IEEE J. Sel. Top. Quant.* **14**, 407 (2008).

[61] M. Yamashita, K. Kawase, and C. Otani. Imaging of large-scale integrated circuits using laser terahertz emission microscopy. *Opt. Express* **13**, 115 (2005).

[62] J. Jackson, M. Mourou, J. Whitaker, I. Duling, S. Williamson, M. Menu, and G. Mourou. Terahertz imaging for non-destructive evaluation of mural paintings. *Opt. Commun.* **281**, 527 (2008).

[63] M. Reid and R. Fedosejevs. Terahertz birefringence and attenuation properties of wood and paper. *Appl. Opt.* **45**, 2766 (2006).

[64] Y. Hu, P. Huang, L. Guo, X. Wang, and C. Zhang. Terahertz spectroscopic investigations of explosives. *Phys. Lett. A* **359**, 728 (2006).

[65] H.-B. Liu, Y. Chen, and X.-C. Zhang. Detection and identification of explosive RDX by THz diffuse reflection spectroscopy. *Opt. Express* **14**, 415 (2006).

[66] B. Ferguson and X.-C. Zhang. Materials for terahertz science and technology. *Nature Mat.* **1**, 26 (2002).

[67] S. L. Dexheimer. *THz spectroscopy: Principles and applications.* CRC Press, Boca Raton, FL (2008).

[68] M. Born and E. Wolf. *Principles of Optics.* Cambridge University Press, Cambridge, 7th edn. (1999).

[69] A. Pashkin. *Terahertz spectroscopy of ferroelectrics and related materials.* Ph.D. thesis, Charles University in Prague, Faculty of Mathematics and Physics (2004).

[70] M. Kempa. *Study of dielectric thin films using time-domain terahertz spectroscopy.* Master's thesis, Charles University in Prague, Faculty of Mathematics and Physics (2003).

[71] J. Petzelt, P. Kužel, I. Rychetský, A. Pashkin, and T. Ostapchuk. Dielectric response of soft modes in ferroelectric thin films. *Ferroelectrics* **288**, 169 (2003).

[72] A. Pashkin, M. Kempa, H. Němec, F. Kadlec, and P. Kužel. Phase-sensitive time-domain terahertz reflection spectroscopy. *Rev. Sci. Instrum.* **74**, 4711 (2003).

[73] S. E. Ralph, Y. Chen, J. Woodall, and D. McInturff. Subpicosecond photoconductivity of $In_{0.53}Ga_{0.47}As$: Intervalley scattering rates observed via THz spectroscopy. *Phys. Rev. B* **54**, 5568 (1996).

[74] A. Leitenstorfer, R. Huber, F. Tauser, A. Brodschelm, M. Bichler, and G. Abstreiter. Femtosecond buildup of Coulomb screening in a photoexcited electron-hole plasma. *Physica B* **314**, 248 (2002).

[75] H. Němec, A. Pashkin, P. Kužel, M. Khazan, S. Schnüll, and I. Wilke. Carrier dynamics in low-temperature grown GaAs studied by THz emission spectroscopy. *J. Appl. Phys.* **90**, 1303 (2001).

[76] H. G. Roskos, M. C. Nuss, J. Shah, K. Leo, D. A. B. Miller, A. M. Fox, S. Schmitt-Rink, and K. Köhler. Coherent submillimetre-wave emission from charge oscillations in a double-well potential. *Phys. Rev. Lett.* **68**, 2216 (1992).

[77] A. Leitenstorfer, S. Hunsche, J. Shah, M. C. Nuss, and W. H. Knox. Femtosecond high-field transport in compound semiconductors. *Phys. Rev. B* **61**, 16 643 (2000).

[78] A. Leitenstorfer, S. Hunsche, J. Shah, M. C. Nuss, and W. H. Knox. Femtosecond charge transport in polar semiconductors. *Phys. Rev. Lett.* **82**, 5140 (1999).

[79] B. B. Hu, E. A. de Souza, W. H. Knox, J. E. Cunningham, M. C. Nuss, A. V. Kuznetsov, and S. L. Chuang. Identifying the distinct phases of carrier transport in semiconductors with 10 fs resolution. *Phys. Rev. Lett.* **74**, 1689 (1995).

[80] B. B. Hu, A. S. Weling, D. H. Auston, A. V. Kuznetsov, and C. J. Stanton. DC-electric-field dependence of THz radiation induced by femtosecond optical-excitation of bulk GaAs. *Phys. Rev. B* **49**, 2234 (1994).

[81] R. D. Averitt, G. Rodriguez, J. L. W. Siders, S. A. Trugman, and A. J. Taylor. Conductivity artifacts in optical-pump THz-probe measurements of $YBa_2Cu_3O_7$. *J. Opt. Soc. Am. B* **17**, 327 (2000).

[82] Z. Mics, F. Kadlec, P. Kužel, P. Jungwirth, S. E. Bradforth, and V. A. Apkarian. Nonresonant ionization of oxygen molecules by femtosecond pulses: plasma dynamics studied by time-resolved terahertz spectroscopy. *J. Chem. Phys.* **123**, 10 4310 (2005).

[83] R. McElroy and K. Wynne. Ultrafast dipole solvation measured in the far infrared. *Phys. Rev. Lett.* **79**, 3078 (1997).

[84] C. A. Schmuttenmaer. Exploring dynamics in the far-infrared with terahertz spectroscopy. *Chem. Rev.* **104**, 1759 (2004).

[85] H. Němec, F. Kadlec, S. Surendran, P. Kužel, and P. Jungwirth. Ultrafast far-infrared dynamics probed by terahertz pulses: a frequency domain approach. I. Model systems. *J. Chem. Phys.* **122**, 10 4503 (2005).

[86] H. Němec, F. Kadlec, and P. Kužel. Methodology of an optical pump-terahertz probe experiment: An analytical frequency-domain approach. *J. Chem. Phys.* **117**, 8454 (2002).

[87] P. Kužel, F. Kadlec, and H. Němec. Propagation of terahertz pulses in photoexcited media: analytical theory for layered systems. *J. Chem. Phys.* **127**, 02 4506 (2007).

[88] M. C. Beard, G. M. Turner, and C. A. Schmuttenmaer. Transient photoconductivity in GaAs as measured by time-resolved terahertz spectroscopy. *Phys. Rev. B* **62**, 15 764 (2000).

[89] H. Němec, F. Kadlec, S. Surendran, P. Kužel, and P. Jungwirth. Ultrafast far-infrared dynamics probed by terahertz pulses: A frequency domain approach. I. Model systems. *J. Chem. Phys.* **122**, 10 4503 (2005).

[90] S. Gupta, M. Y. Frankel, J. A. Valdmanis, J. F. Whitaker, G. A. Mourou, F. W. Smith, and A. R. Calawa. Subpicosecond carrier lifetime in GaAs grown by molecular beam epitaxy at low temperatures. *Appl. Phys. Lett.* **59**, 3276 (1991).

[91] K. P. H. Lui and F. A. Hegmann. Ultrafast carrier relaxation in radiation-damaged silicon on sapphire studied by optical-pump–terahertz-probe experiments. *Appl. Phys. Lett.* **78**, 3478 (2001).

[92] E. Knoesel, M. Bonn, J. Shan, and T. F. Heinz. Charge Transport and Carrier Dynamics in Liquids Probed by THz Time-Domain Spectroscopy. *Phys. Rev. Lett.* **86**, 340 (2001).

[93] S. R. Elliott. A.c. conduction in amorphous chalcogenide and pnictide semiconductors. *Adv. in Phys.* **36**, 135 (1987).

[94] P. Prins, F. C. Grozema, J. M. Schins, and L. D. A. Siebbeles. Frequency dependent mobility of charge carriers along polymer chains with finite length. *Phys. Stat. Sol.(b)* **243**, 382 (2006).

[95] J. C. Dyre. The random free-energy barrier model for ac conduction in disordered solids. *J. Appl. Phys.* **64**, 2456 (1988).

[96] R. Huber, F. Tauser, A. Brodschelm, M. Bichler, G. Abstreiter, and A. Leitenstorfer. How many-particle interactions develop after ultrafast excitation of an electron-hole plasma. *Nature* **414**, 286 (2001).

[97] R. A. Kaindl, M. A. Carnahan, D. Hagele, R. Lovenich, and D. S. Chemla. Ultrafast terahertz probes of transient conducting and insulating phases in an electron-hole gas. *Nature* **423**, 734 (2003).

[98] T. I. Jeon and D. Grischkowsky. Nature of Conduction in Doped Silicon. *Phys. Rev. Lett.* **78**, 1106 (1996).

[99] M. Levinshtein, S. Rumayantsev, and M. Shur. *Handbook Series on Semiconductor Parameters*, vol. 2. Singapore: World Scientific (1999).

[100] R. Jacobsson. *Light Reflection from Films of Continuously Varying Refractive Index*, vol. V of *Progress in Optics*, chap. 5. North-Holland, Amsterdam (1965).

[101] F. Kadlec, H. Němec, and P. Kužel. Optical two-photon absorption in GaAs measured by optical pump-terahertz probe spectroscopy. *Phys. Rev. B* **70**, (2004).

[102] F. L. Pedrotti and L. S. Pedrotti. *Introduction to Optics*. Prentice Hall, Englewood Cliffs, 2nd edn. (1993).

[103] H.-T. Chen, W. J. Padilla, J. M. O. Zide, S. R. Bank, A. C. Gossard, A. J. Taylor, and R. D. Averitt. Ultrafast optical switching of terahertz metamaterials fabricated on ErAs/GaAs nanoisland superlattices. *Opt. Lett.* **32**, 1620 (2007).

[104] W. J. Padilla, D. N. Basov, and D. R. Smith. Negative refractive index metamaterials. *Materials Today* **9**, 28 (2006).

[105] W. J. Padilla, M. T. Aronsson, C. Highstrete, M. Lee, A. J. Taylor, and R. D. Averitt. Electrically resonant terahertz metamaterials: Theoretical and experimental investigations. *Phys. Rev. B* **75**, 04 1102 (2007).

Appendix

[i] H. Němec, L. Fekete, F. Kadlec, P. Kužel, M. Martin, J. Mangeney, J. Delagnes, and P. Mounaix. Ultrafast carrier dynamics in Br^+-bombarded InP studied by optical-pump terahertz-probe spectroscopy. *Phys. Rev. B.* Accepted.

[ii] L. Fekete, P. Kužel, H. Němec, F. Kadlec, A. Dejneka, J. Stuchlík, and A. Fejfar. Ultrafast carrier dynamics in microcrystalline silicon probed by time-resolved terahertz spectroscopy. *Phys. Rev. B.* Submitted.

[iii] L. Fekete, H. Němec, F. Kadlec, P. Kužel, J. Stuchlík, A. Fejfar, and J. Kočka. Carrier dynamics in microcrystalline silicon studied by time-resolved terahertz spectroscopy. *J. Non-Cryst. Solids* **352**, 2846 (2006).

[iv] L. Fekete, J. Y. Hlinka, F. Kadlec, P. Kužel, and P. Mounaix. Active optical control of the terahertz reflectivity. *Opt. Lett.* **30**, 1992 (2005).

[v] L. Fekete, F. Kadlec, P. Kužel, and H. Němec. Ultrafast opto-terahertz photonic crystal modulator. *Opt. Lett.* **32**, 680 (2007).

[vi] L. Fekete, F. Kadlec, H. Němec, and P. Kužel. Fast one-dimensional photonic crystal modulators for the terahertz range. *Opt. Express* **15**, 8898 (2007).